ANALYSIS AND CLASSIFICATION OF TWO MULTI-LAYERED DEPOSITS, XANTHE TERRA, MARS

By

Charlotte P. Tierney

A thesis submitted in partial fulfillment

of the requirements for the degree of

MASTER OF SCIENCE

in

Geosciences

Middle Tennessee State University

May 2020

ACKNOWLEDGEMENTS

Thank you to my advisors, Henrique, Joe, and Jeremy,

for keeping me on track and believing in me as

we figured out the thesis process and

throughout my time at MTSU.

Thank you to Mom, Dad, Nani, and Bop for… everything.

Thank you to my Sisters[2] for support and puppy snaps;

to Spencer for listening, editing, and understanding my brain;

to Connor for encouragement, joy, and perfectly distracting content;

and to Katy and Sarah for being the best people to share grad school with.

ABSTRACT

The Orson Welles Chaos is a linear feature located between the Orson Welles crater and Ganges Chasma in Xanthe Terra, Mars. Within the Chaos system there are two neighboring deposits of white sediment that are uniquely colored and horizontally layered in visible light imagery. Geomorphic features are qualitatively, statistically, and spatially analyzed using High-Resolution Imaging Experiment imagery. Spectral signatures are measured and compared using Compact Reconnaissance Imaging Spectrometer for Mars hyperspectral data.

This study looks at the potential role of water in the formation of the study sites. The layers at the study sites might have been formed by hydrous minerals, show some hints of shoreline drop-offs, and may have topography for paleochannels, but evidence is inconclusive overall. Dune pattern analysis shows modern wind patterns might have changed recently and definitively shows multiple surface ages. The history of these sites informs the geologic and hydrologic history around the Mars equator.

TABLE OF CONTENTS

LIST OF TABLES

LIST OF FIGURES

LIST OF FIGURES

(continued)

LIST OF COMMON ABBREVIATIONS

DEM – Digital Elevation Model

HiRISE – High-Resolution Imaging Experiment

CTX – Context Camera

CRISM – Compact Reconnaissance Imaging Spectrometer for Mars

ROI – Region of interest

CHAPTER I

INTRODUCTION

Location and Geologic History

The Orson Welles Chaos is a linear feature located between the Orson Welles crater and Ganges Chasma in Xanthe Terra, Mars. Orson Welles crater is located at -0.19N, 314.1E. The Orson Welles Chaos (the Chaos) is located just below the equator and extends 280 kilometers south-southwest and is 70 kilometers wide (see Figure 1). Within the Chaos there are features such as scarps, landslide deposits, linear and barchan dunes, extensional and *en echelon* faults, grabens, collapsed pits, and craters.

The postulated formation of the Chaos began with larger planet-wide processes and slowed with the aridification of the Mars environment circa 3.7 giga-annum (Ga). When the Tharsis Superplume was active, the region nearly 4,000 kilometers west of the Chaos was uplifted and created radial faults that extend through the hemisphere and through the extensional faults in Xanthe Terra (Mutch et al., 1976; Carr, 1981). Mutch et al. (1978) states that most of the chasms on the Tharsis hemisphere were likely formed in part by the faulted crust, in which water could travel and later erode. These intersecting faults possibly made the surface between the Orson Welles crater and Ganges Chasma weaker (C in Figure 1b). In that space, there was an aquifer or cryosphere layer filled by northward drainage of a paleolake in Ganges Chasma (Cabrol et al., 1997) (D in Figure 1b). Cabrol et al. (1997) hypothesized that when the cryosphere melted—possibly due to magmatic intrusion or geothermal heating (Rodriguez et al., 2003)—the water drained from the aquifer into the Orson Welles crater and northward into Shalbatana Vallis. Figure 2 shows the geologic timescale of Mars and the modeled atmospheric conditions. The combined

(**a**)

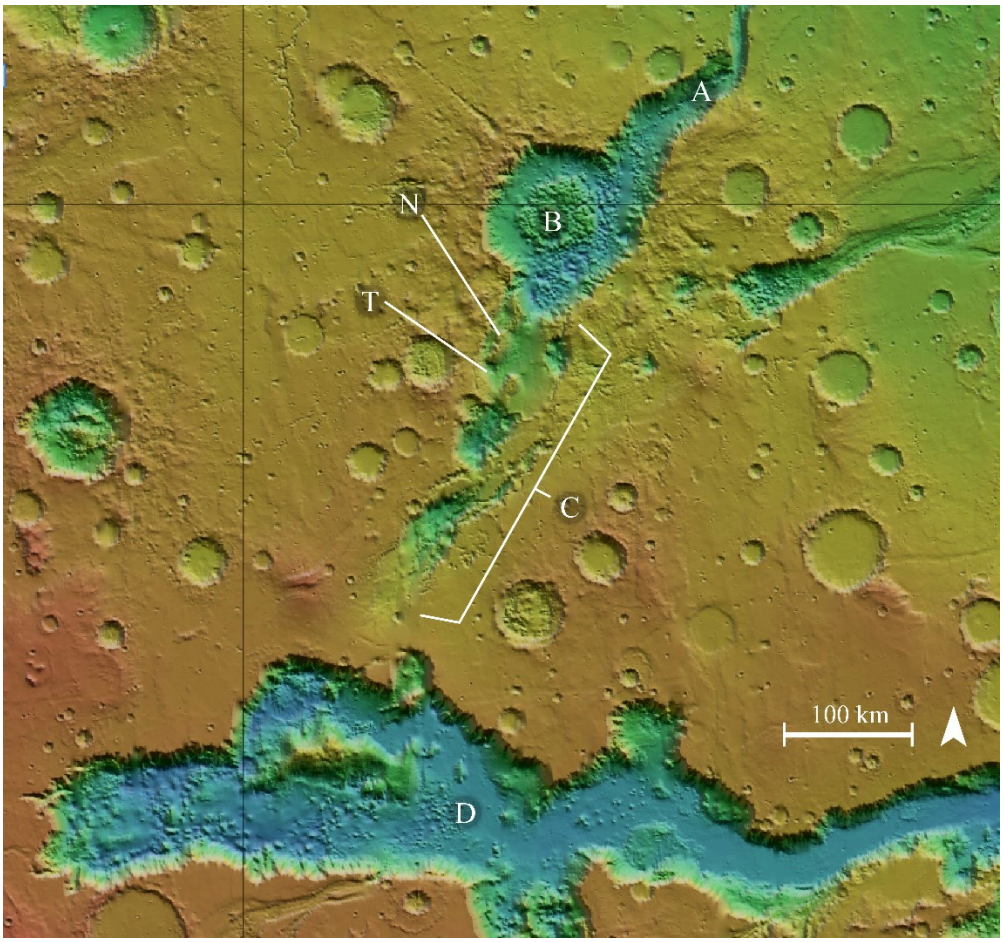

(**b**)

Figure 1. (**a**) Study site location at a planet-wide scale. Vallis Marineris is center in this image. (**b**) The Orson Welles Chaos and the surrounding area at a more local scale. In inset b, *A* is Shalbatana Vallis, *B* is the Orson Welles crater, *C* is the Chaos, *D* is Ganges Chasma, *T* is the location of Crater T, and *N* is the location of Site N. Background image from JMARS, NASA/JPL-Caltech/Arizona State University.

ideas of Cabrol et al. (1997) and Rodriguez et al. (2003) suggest that the drainage of the aquifer caused the collapse of the subsurface caverns and created the chaotic terrain of the Orson Welles Chaos.

Within the Chaos system there are two neighboring deposits of white sediment that appear very different from the surrounding brown sediment in visible light imagery. Site N (Figure 3) and Crater T (Figure 4) are the study sites of this investigation. These sites are located about 40 kilometers apart in the northwest part of the Chaos (Figure 1b). Crater T is 9 kilometers in diameter and the floor sits about 1,700 meters below the mean Martian elevation. Site N is about 1,000 kilometers below average. Both of these sites have the uniquely colored and layered sediment deposits. At Site N and Crater T there are linear dunes made of only brown sediment (Figures 5 and 6). The layers, sorting, morphology, and apparent stability of this sediment deposit make it different from the area around it and create complexities in the formation models of the area. Because this sediment is exposed at only two locations in the nearly 20,000 square kilometers of the Orson Welles Chaos, understanding its deposition will impact the history of the collapse zone and possibly the history of liquid surface water in Xanthe Terra and around the Mars equator.

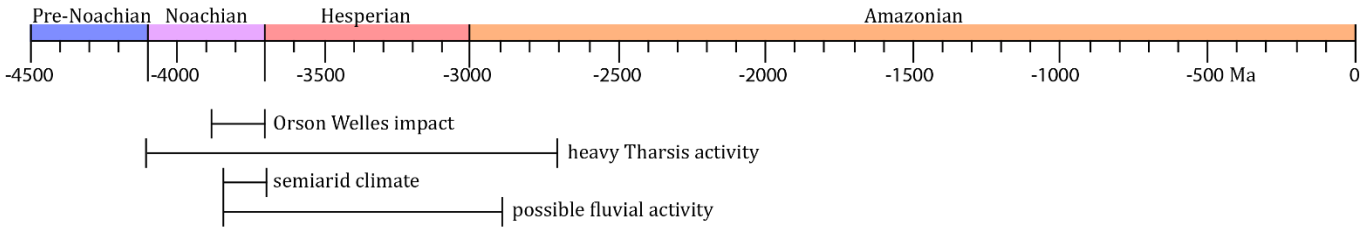

Figure 2. Mars geologic timescale, showing the windows for the Orson Welles impact, heavy Tharsis activity, and the general Martian climate (Cabrol, Grin, & Dawidowicz, 1997; Dohm et al., 2015; Horvath & Andrews-Hanna, 2017). The collapse of the Orson Welles Chaos likely happened in the Hesperian Era.

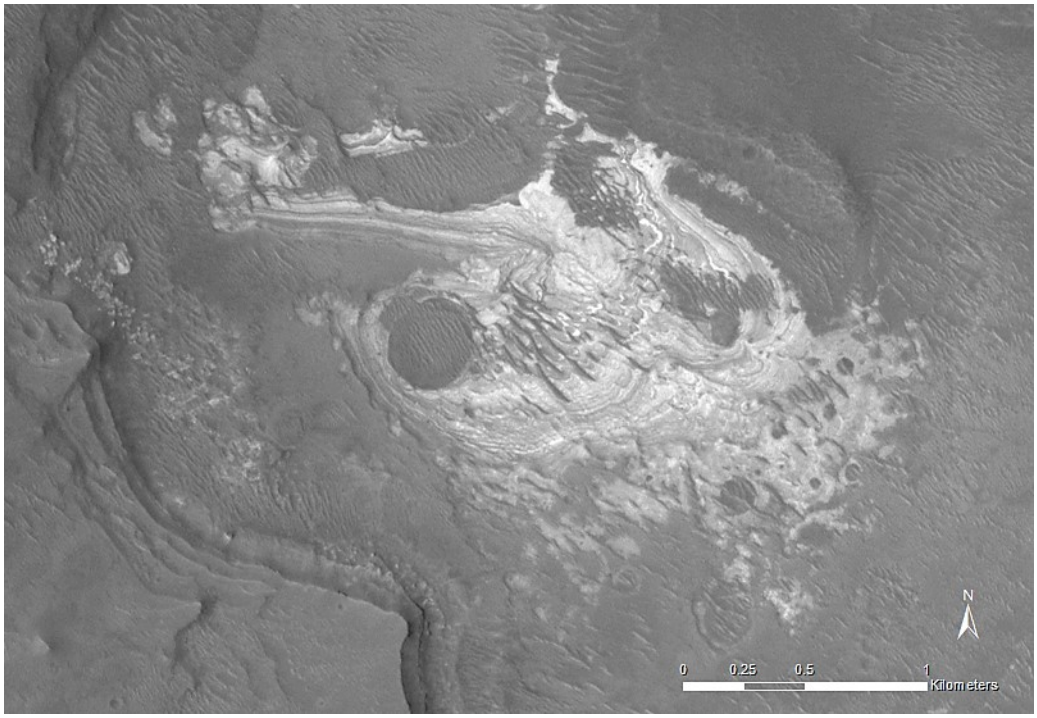

Figure 3. CTX image of Study Site N, featuring the white sediment in clear layers.

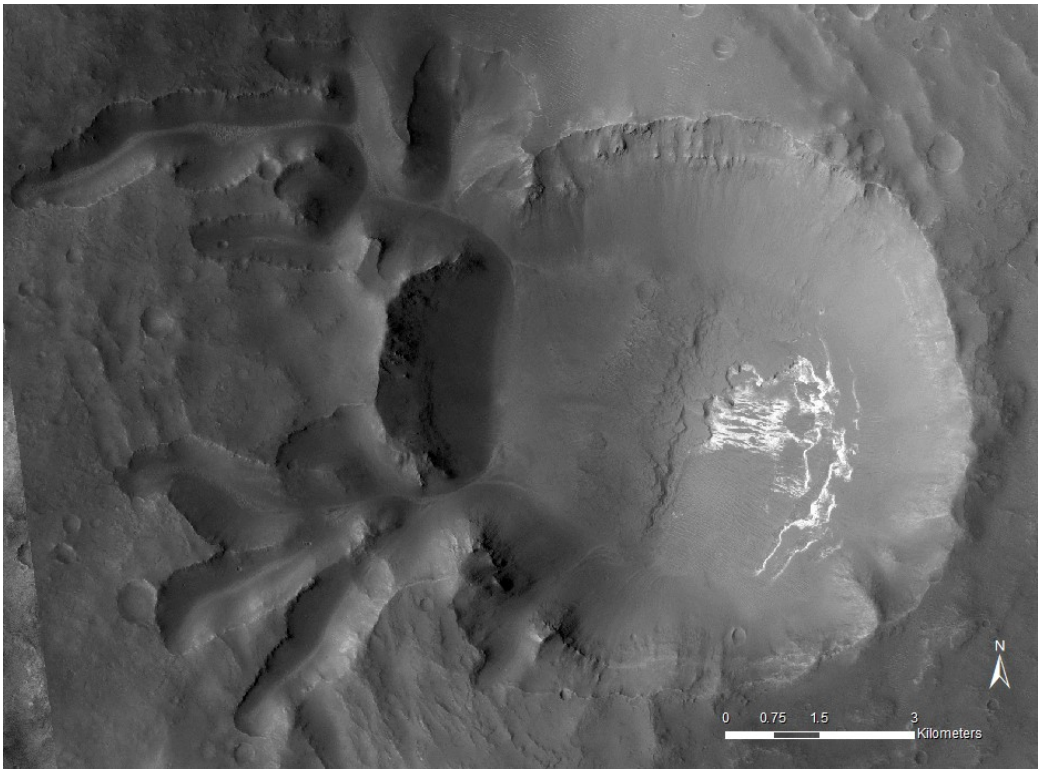

Figure 4. CTX image of Crater T, featuring the white sediment deposit in the crater floor, shaded by sunlight. The crater is about 9 km in diameter.

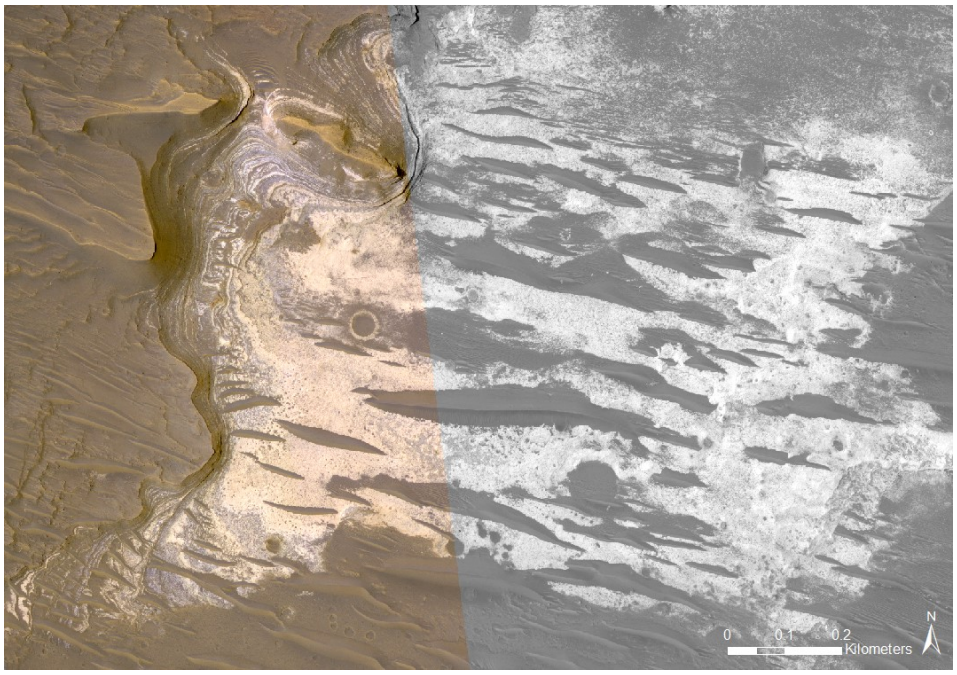

Figure 5. A close-up of the sediment on the floor of Crater T from HiRISE. Visible are dunes made of only brown sediment, layers of alternating brown and white sediment in the paleo toe scarps, and good sorting of the different types of sediment.

Figure 6. A close-up of the sediment layers at Site N from HiRISE. Visible are dunes made of only brown sediment and layers of alternating brown and white sediment. The lines and patterns of Site N are considerably different from the floor of Crater T (in Figure 5).

Objectives

This research project aims to understand the sediment layers at Site N and Crater T using remote sensing to analyze geomorphology and spectrometry. This study has two main objectives: first, to qualitatively and quantitatively analyze the topography and geomorphology of the study sites, including conducting a pattern analysis of the dune fields within both sites and second, to determine the potential mineral composition of the white and brown sediments to constrain formation conditions of the sediment layers. The geomorphic analysis yields insight into both historic and modern processes at each site. The mineral composition of this sediment holds major clues about the history of the Chaos and formation conditions of the sediment layers. There are many implications and questions to explore based on the type of minerals found in the sediment.

To accomplish these objectives, remotely sensed high spatial-resolution data and hyperspectral data were analyzed. The combination of geomorphology and spectrometry will aid in constructing a hypothesis regarding the formation mechanisms of the layered sediment deposits and the surrounding structures in Site N, Crater T, and in the larger Orson Welles Chaos. Therefore, the hypothesis of this study is that there is a relationship between the geomorphology and mineral composition and the brown and white layered sediment deposits.

CHAPTER II

METHODS

Study Tools

All published data used in this study was generated by remote sensors. The primary spacecrafts for these tools are the Mars Global Surveyor (MGS) and the Mars Reconnaissance Orbiter (MRO). These orbiters are operated primarily by NASA. Data is processed and made available to the public by various universities and laboratories, including NASA, Johns Hopkins University Applied Physics Lab (JHUAPL), University of Arizona (UA) Lunar and Planetary Laboratory (LPL), the Planetary Image Locator Tool (PILOT) by the United States Geologic Survey (USGS), the Planetary Data Systems (PDS) Geosciences Node from Washington University in St. Louis (UWSL), and Arizona State University (ASU). The data can be navigated using the Java Mission-planning and Analysis for Remote Sensing (JMARS) geographic information system by Arizona State University (Christensen et al., 2009).

The Mars Global Surveyor is the spacecraft for the Mars Orbital Laser Altimeter (MOLA). MGS began mapping Mars in 1999 and finished its mission in 2006. MOLA was one of five instruments included on the spacecraft and collected laser altimetry data for the whole planet at 10 hertz and a spatial resolution of around 170 meters (which improved during the extended mission). MOLA data was used to generate topographic maps and digital elevation models (DEMs) of the entire planet (NASA MGS, n.d.).

The Mars Reconnaissance Orbiter is the spacecraft for the Context Camera (CTX), High-Resolution Imaging Experiment (HiRISE), and the Compact Reconnaissance Imaging Spectrometer for Mars (CRISM) sensors. The MRO has been orbiting the planet since 2006 and was a groundbreaking launch of telecommunication systems and high-definition cameras. CTX

has a spatial resolution of about 6 meters per pixel and has imaged the entire planet (replacing the imaging done by MGS and Odyssey). HiRISE has a spatial resolution of about 25 centimeters per pixel and has collected data on specific features on the planet. HiRISE targets were originally selected using data from the Mars Global Surveyor and the Mars Odyssey. Targets are now chosen by researchers all over the world and are often based on CTX data. HiRISE is operated by the Lunar and Planetary Laboratory at the University of Arizona. CRISM produces two images for each location it analyzes—one visible-near-infrared and one infrared. The spectrometer covers a spectral range from 362-3920 nanometers with a spectral sampling of 6.55 nanometers per channel. These images have a spatial resolution of about 20 meters (NASA MRO, n.d.).

This study collected spectroscopy, visible light, and topographic data from the MRO CRISM spectrometer, MRO HiRISE and CTX cameras, and MGS MOLA data. Table 1 describes the collected data sets from CTX, CRISM, HiRISE, and MOLA.

Table 1. Collected data products and specifications.

Sensor	Data Type	Scene	Study Site	Date Collected	Spatial Resolution	Spectral Resolution	Data Source
CTX	Image	J06_047014_1784_XI_01S046W	N	8/2016	5.28 m/px	1 band 500 - 800 nm	PILOT
	Image	J04_046447_1777_XI_02S046W	T	6/2016	5.26 m/px		
CRISM	Spectroscopy	0000A280	N	2/2008	20 m/px	430 bands 362 - 3920 nm	PDS
	Spectroscopy	00008EBF	T	12/2007	20 m/px		
HiRISE	Image	PSP_007455_1785	N	2/2008	26.8 cm/px	3 bands BG: 400 - 600 nm R: 550 - 850 nm NIR: 800 - 1000 nm	LPL
	Image	ESP_033458_1785	N	9/2013	29.5 cm/px		
	Image	PSP_006598_1780	T	12/2007	26.7 cm/px		
	Image	ESP_033326_1780	T	9/2013	59.6 cm/px		
	DEM	DTEEC_007455_1785_ 033458_1785_A01	N		1.01 m/px		
	DEM	DTEEC_033326_1780_ 006598_1780_A01	T		1.01 m/px		
MOLA	DEM	MGS MOLA DEM 463m v2	Chaos	1999-2001	463.09 m/px	1.064 μm at 10 Hz	PDS

Data was processed using ENVI Classic + IDL, ENVI 5.5, and ArcMap 10.6.1 for the exploration of reflectance and radiance, mapping of geomorphic features, and understanding of topography.

Geomorphology

Understanding the topography and geomorphology of the study sites will possibly yield insights into the history of the region. Key features of each study site were mapped, analyzed spatially and statistically, and compared. This study measured elevation, dune fields, potential shorelines, sedimentary bedding, the sorting of sediment, and relative ages of features around the sediment layers. Analysis of the study sites was conducted using CTX and HiRISE images and HiRISE DEMs. Features were analyzed to understand the sand supply, wind direction, erosion, and material within the crater.

Study sites were analyzed using the HiRISE 1 meter digital elevation model, which has a spatial resolution sufficient for moderate scale studies but has occasional interpolation errors at some locations (Figure 7). Parameters for analysis and mapping were chosen based on availability of data and site-specific research questions.

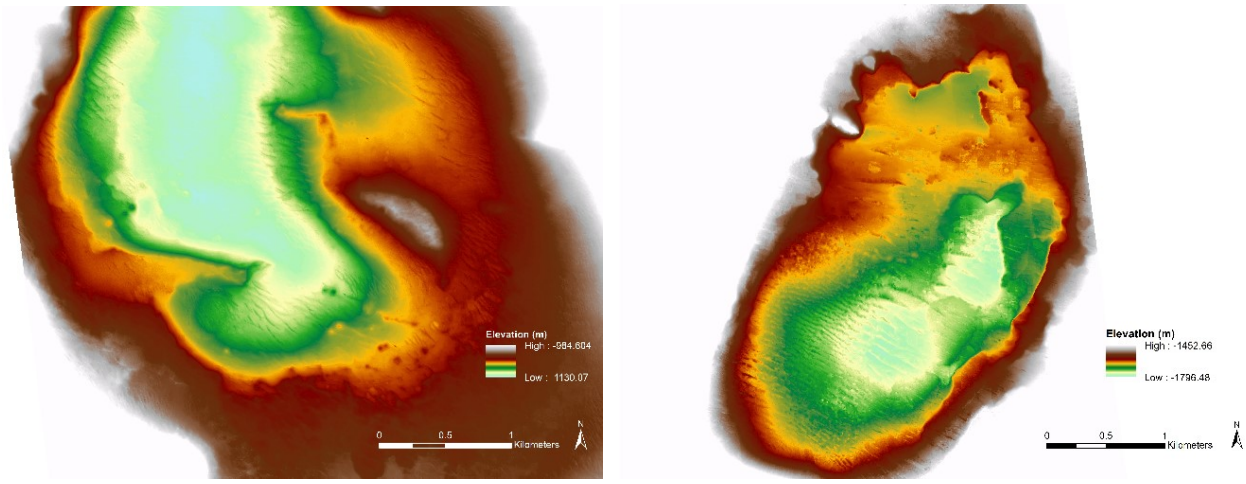

(a) **(b)**

Figure 7. Digital elevation models for Site N (**a**) and Crater T (**b**), symbolized to highlight the changes in elevation at low elevations in the basins.

Wherever sediment layers were exposed in the imagery *and* the DEM showed a change in elevation, profile lines were interpolated for Crater T. The topographic profiles were then compared to the visible layers for any correlation between elevation change and sediment color.

Ripple migration and dune movement is happening on Mars (Bridges et al., 2012; Chojnacki, Banks, Fenton, & Urso, 2019; Silvestro, Fenton, Vaz, Bridges, & Ori, 2010). Studies have been done to analyze the causes and rates of this aeolian movement (Chojnacki et al., 2019; Fenton, Bandfield, & Ward, 2003; Sullivan & Kok, 2017), but many of the investigated processes—such as sand supply, sand fluxes, and wind—are more complex at Site N and Crater T due to their relatively low elevations. Documentation from the University of Arizona states that some HiRISE data can be classified as "change detection images" to quantify surface change at close scales. The collected images are not classified as such but have been used to manually look for changes in dune movement, slope advancement or retreat, and new craters. Change detection was done at both study sites qualitatively using the PSP and ESP HiRISE images at each site.

The basin of Crater T was analyzed for a possible shoreline, which could serve as evidence of standing water. Qualitative analysis of the basin images suggests features that look like shorelines from a map view but could not be confirmed without elevation data. Using the HiRISE DEM, contour lines were created and compared to visible changes in topography. Elevation data used for this analysis was carefully checked for errors before being included. Interpolated lines were drawn over possible shorelines or steep changes in topography, as identified in imagery and in the elevation model. The topographic profile of each line was manually analyzed for a distinct drop-off and clean DEM data. Where the change in elevation was distinct and clear, a polyline was drawn with the drop-off elevation documented with the feature attribute.

The dune fields in the basins and near the sediment layers were studied at both locations. Typical diagnostic spatial features used in dune pattern recognition include dune spacing, crest orientation, crest length, and defect density (Lancaster, 1994). Previous research has shown that statistical analyses of these variables can aid in interpretation of episodic dune activity, changing wind regimes, timing and magnitude of aeolian events, and for dating episodes of dune formation in a complex dune pattern due to their time dependence (Ewing, Kocurek, & Lake, 2006; Ritter, Kochel, & Miller, 2011).

Methods for dune pattern analysis were measured similarly to Ewing et al. (2006). The location for dune analysis at both sites was chosen based on qualitative observations of dune shapes and elevation. Polylines were drawn manually over the dune crests visible in the HiRISE images. The length geometry was calculated for each dune crest in the attribute table, the straight-line distance of each dune was calculated using a Visual Basic script and the start and end coordinates of each crest, and then the sinuosity of each dune was computed.

The small dune field in the lowest elevations of Crater T was analyzed in more detail due to the apparent youthful age of the dunes compared to the surrounding surface. Seven transect lines were drawn perpendicular to the dunes, approximately 200 meters apart. Intersecting the transects and the dune crest lines yielded a point dataset that was analyzed to determine the distances between each dune crest along the transect lines. The topography data from the DEM was added to the intersect point layer to measure the elevation of the dune along the transect lines. The cardinal direction of each dune was calculated using a VB script and the inverse tangent of the line made by the start and end coordinates.

The relative height of each dune was taken by adding points to the original point dataset at approximately 1 meter of separation and assigning elevation values to newly added points. Dune

height was calculated by subtracting the lowest elevation from the highest elevation for both sides of each dune, then taking the average.

Ewing et al. (2006) define dune defects as breaks in the dune pattern or terminations of a dune. This study defines dune defects as a split or break in the dune crest or an apparent loop (Figure 8). Ewing et al. (2006) use the number of defect pairs on each crestline to define defect density; this study uses distance to the nearest defect point to calculate defect density. Defects were manually marked with points in ArcMap and distances from one point to the nearest defect point were computed using the Near tool.

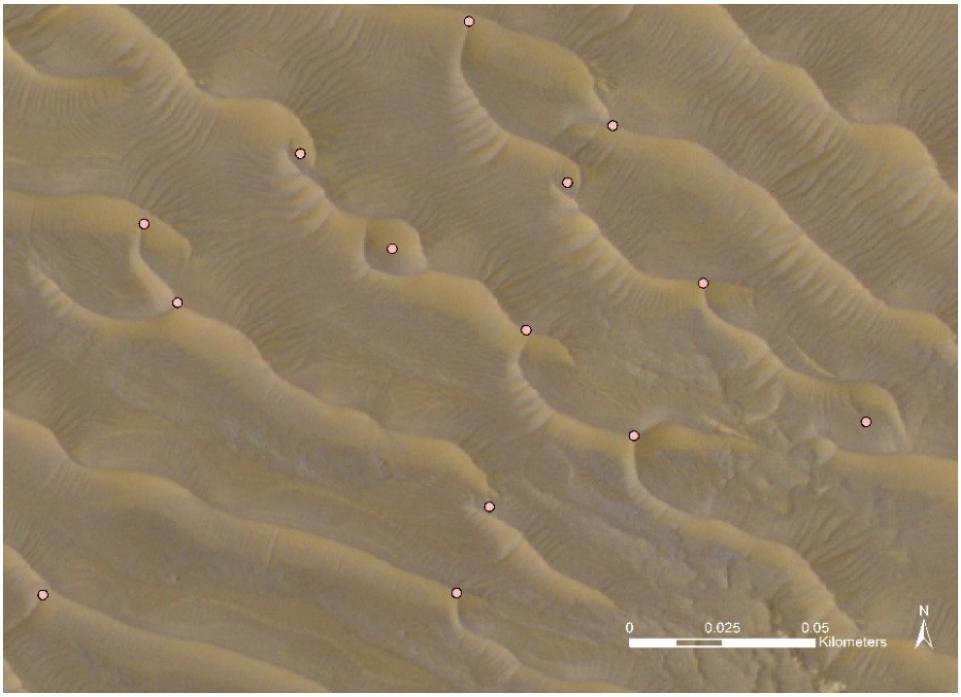

Figure 8. Defect points in Crater T, defined by splits and loops in dune crest lines.

Spectrometry and Mineral Analysis

In visible light, these sediments are very different, which is the primary inspiration for this study. Figures 9 and 10 show the study sites in visible light from the CRISM hyperspectral images.

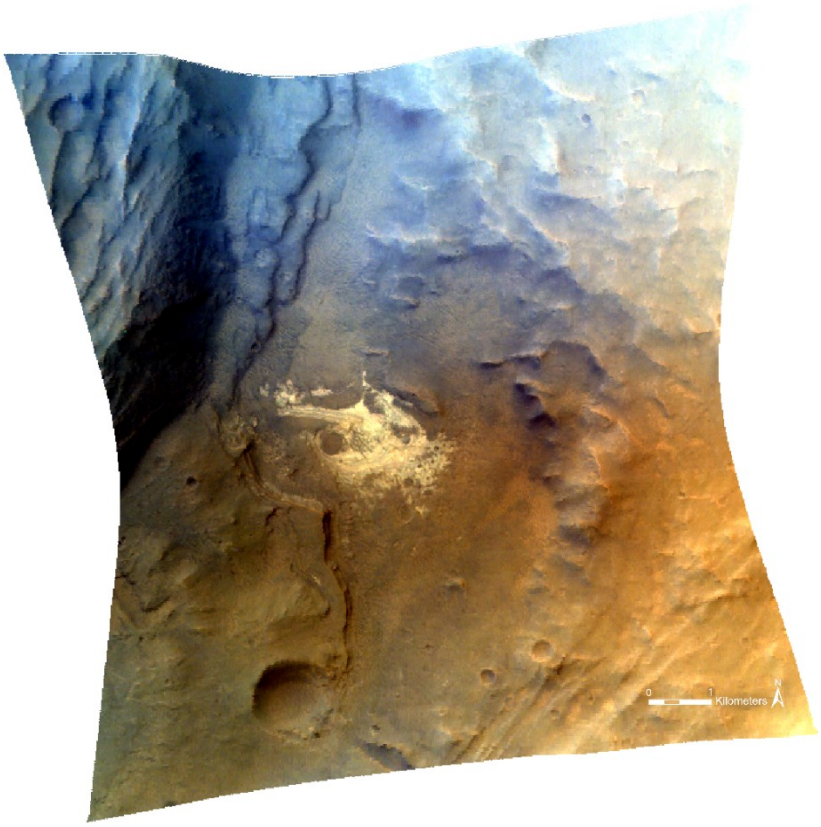

Figure 9. The projected CRISM data file in visible-near-infrared light for Site N, displayed with a linear stretch and RGB canons set at bands 42, 27, and 13, respectively.

Spectral data holds major clues about the history of the Chaos and the formation conditions of the sediment layers. Because minerals often have very specific formation conditions, using spectral analysis to identify minerals will isolate the possibilities for deposition of the sediment layers at Site N and Crater T. For example, finding hydrated or precipitated minerals would imply

the existence of surface water in the study sites; igneous minerals would mean the sediments may be an indicator of local magmatism or may have been transported from a more volcanically active area. Analyzing the hyperspectral data of the study sites adds context for the deposition and exposure history of the area. Spectral data was collected by the MRO CRISM instrument, accessed through the JHUAPL CRISM Data Products website, and processed using ENVI Classic + IDL with the CRISM Analysis Toolkit (CAT), and ENVI 5.5.

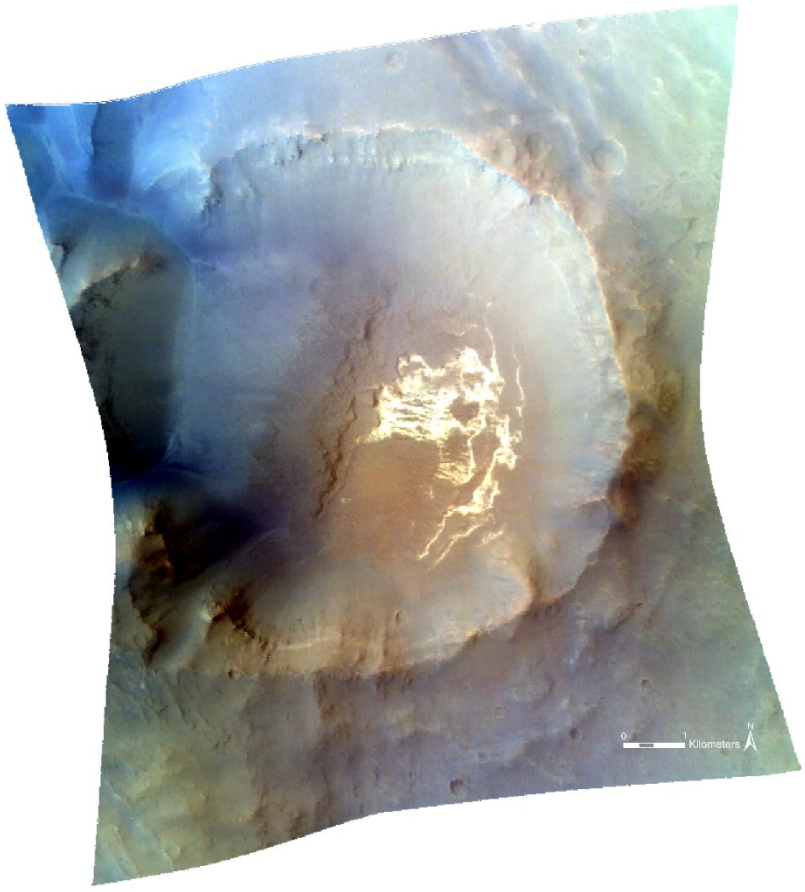

Figure 10. The projected CRISM data file in visible-near-infrared light for Crater T, displayed with a linear stretch and RGB canons set at bands 42, 27, and 13, respectively.

To analyze the data for both Site N and Crater T, the data provided by the PDS for each site (targeted reduced data records and derived data records) were projected into single cube data in ENVI CAT—this projected the hyperspectral images and combined the wavelength metadata to a file that was readable in ENVI 5.5. This process was done for the visible-near infrared (VNIR) and infrared (IR) data files at both sites. Once processed, each site was opened in ENVI 5.5. Five regions of interest (ROIs) were selected for both sediment types at both sites (see Figures 11 and 12). Each ROI, 20 in total, was the size of one pixel, which has a spatial resolution of 18 meters. ROIs were selected based on visual comparison to the HiRISE images for each location—the 25 cm/pixel HiRISE data allowed ROI selection to focus on locations for the brown and white sediments that were as uncontaminated by the other sediment type as possible. Unfortunately, due to the spatial resolution of the CRISM data and the deposition of the white sediment, the white sediment pixels are not likely to be pure pixels. Spectral signatures were collected at each ROI with both the VNIR file and the IR file. The spectral signatures for each type of sediment, at each location, were averaged and merged for graphical visualization. Spectral Analyst was processed using the averaged spectral data to identify minerals with similar spectra.

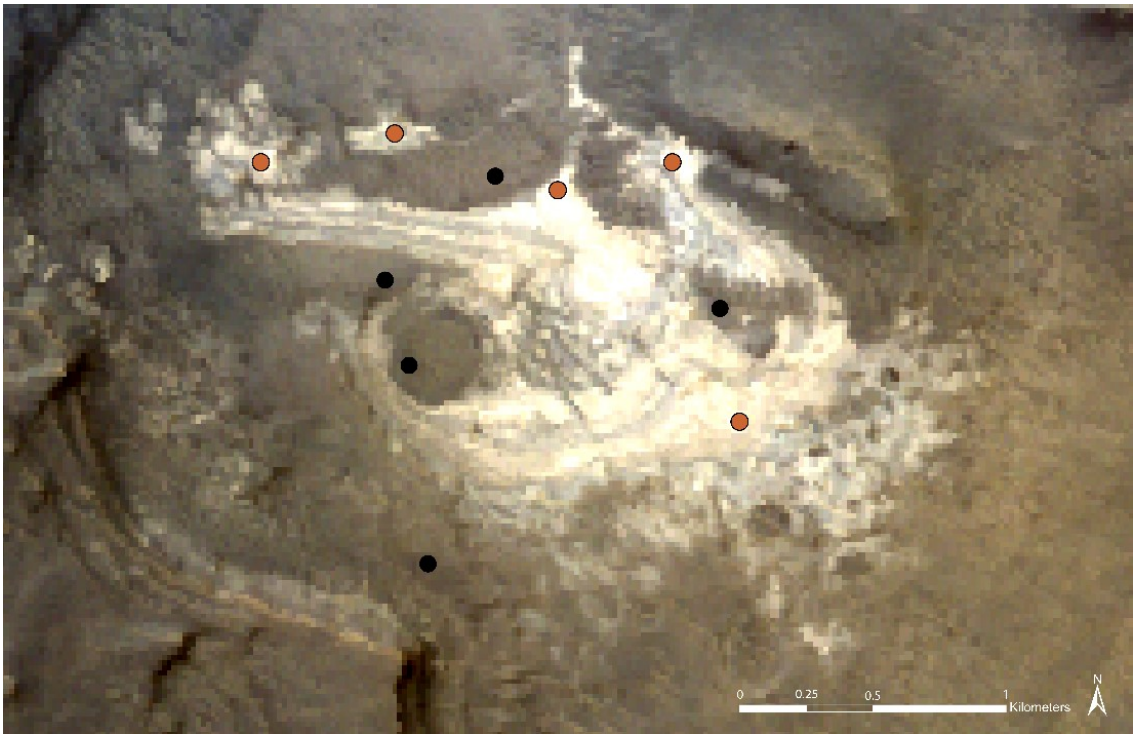

Figure 11. Locations for the selected regions of interest at Site N. Orange dots represent white sediment locations; black dots represent brown sediment locations.

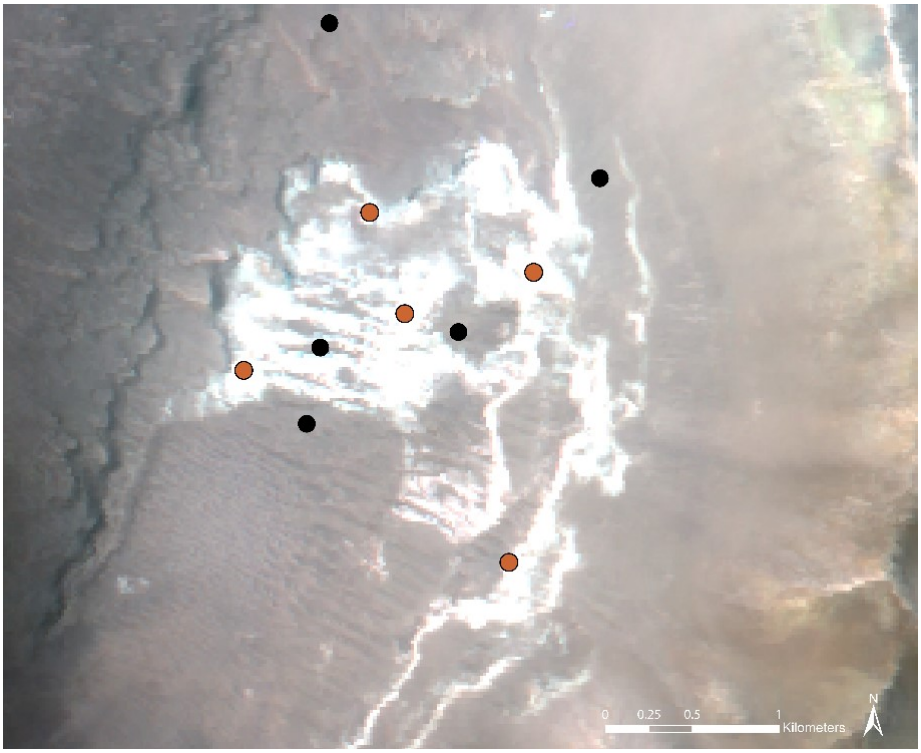

Figure 12. Locations for the selected regions of interest at Crater T. Orange dots represent white sediment locations; black dots represent brown sediment locations.

CHAPTER III

RESULTS

Geomorphology

The overall topography of each study site shows that the white sediment layers exist in basins. Larger collapsed pits surround the study sites, but the two exposures of white sediment are in more isolated basins (Figure 13).

The rim of Crater T is noticeably lopsided (Figure 14). The crater is superimposed on the larger basin, so the impact occurred after the collapse of the Orson Welles Chaos. The eastern crater wall is within the larger pit and the western wall is on the edge of the larger pit. The western wall of Crater T has collapsed, filling in the basin, likely because of the tilt toward the larger collapsed basin. Based on the morphology of the surface and impact crater density, much of that mas wasting scarp (visible in in Figure 14b) stabilized and became compacted. The layers within likely formed after the impact but before the mass wasting, as they would not have maintained their precise layers through an impact event.

The origin of the morphology at Site N is less certain than an impact crater, but the morphology mimics how water can erode smaller sediments (Figure 15).

Figure 13. The location of Site N and Crater T with visual imagery and elevation data from HiRISE. Both sites are in basins relative to their local surroundings.

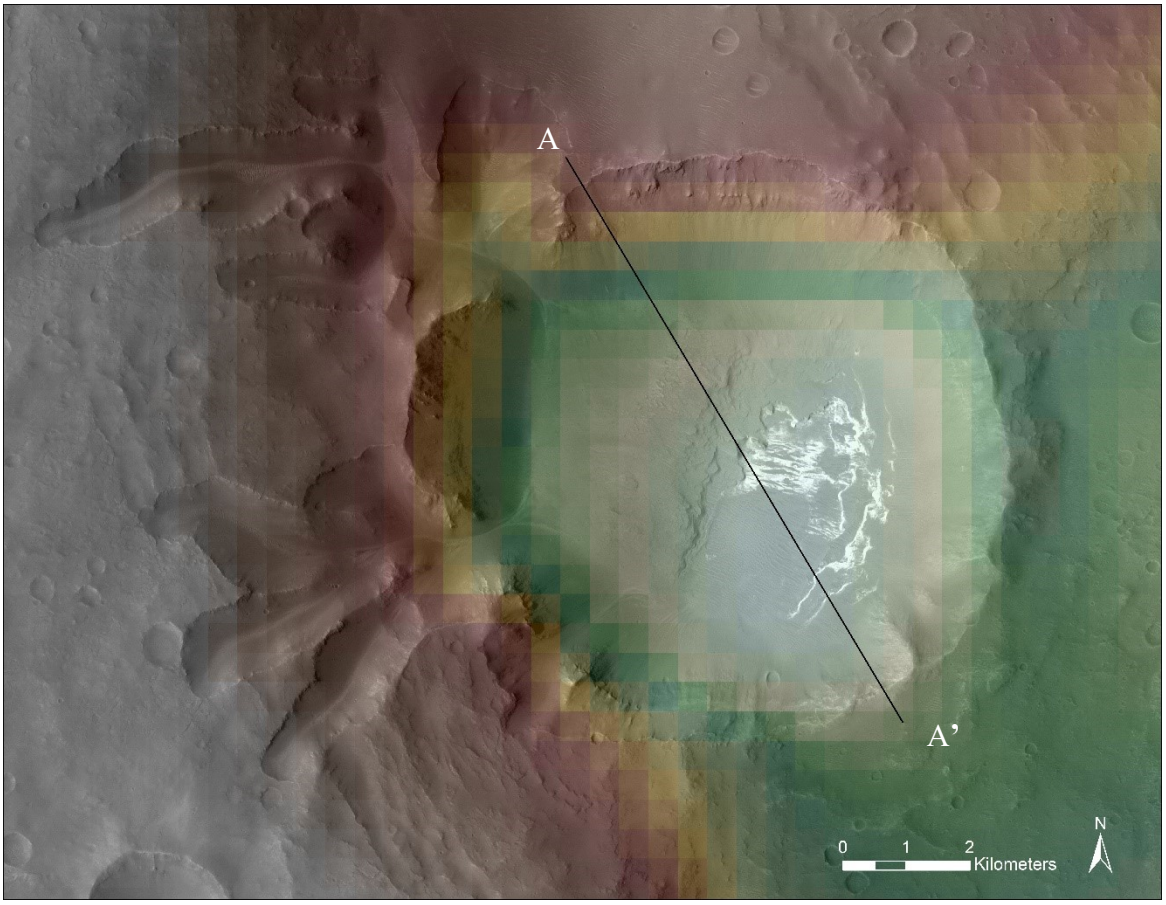

(**a**)

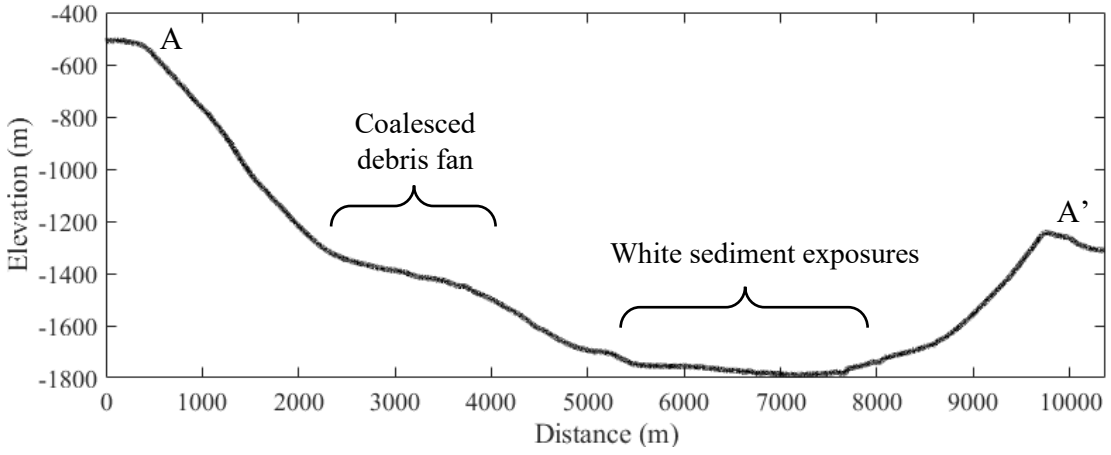

(**b**)

Figure 14. A NW/SE profile of Crater T. (**a)** The location of the profile. (**b**) The elevation profile line. The change in elevation from the northwestern wall to the southeastern wall is nearly 700 meters. The white sediment is located in the lowest elevations, around -1750m.

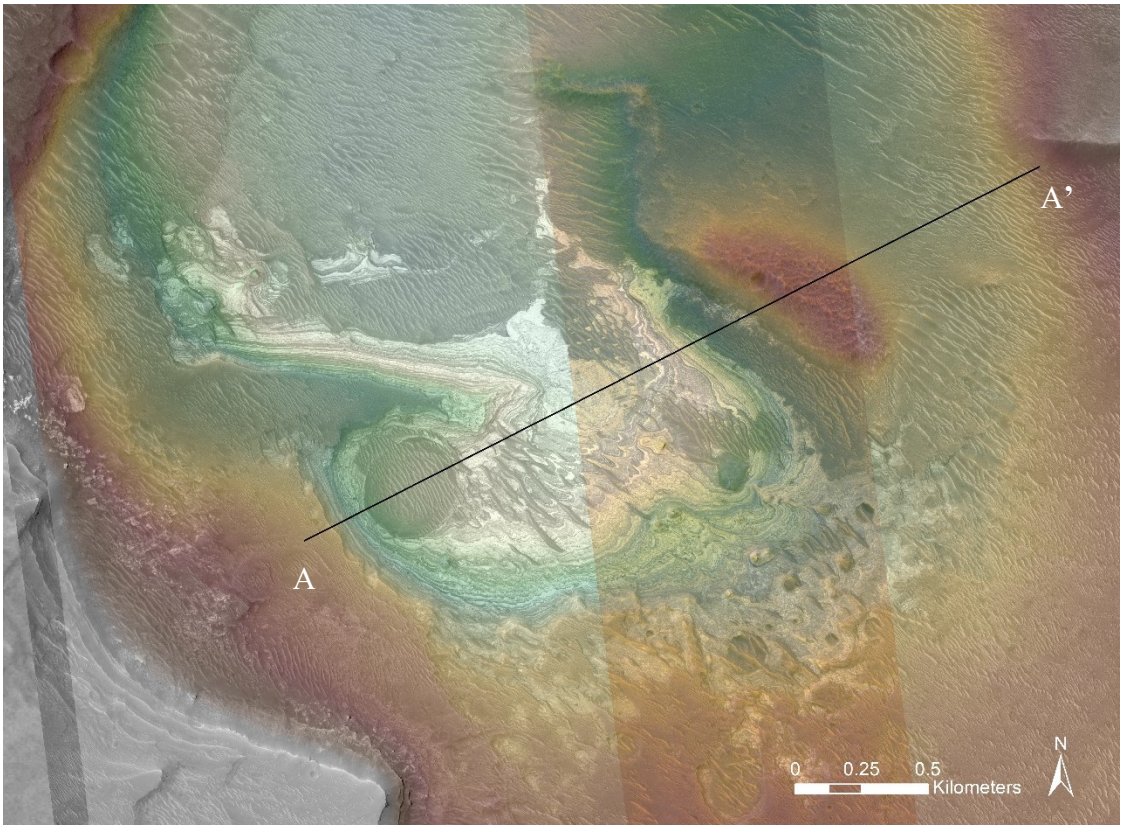

(**a**)

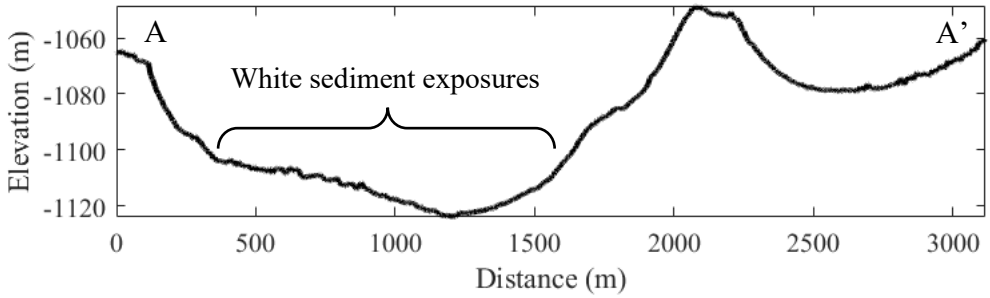

(**b**)

Figure 15. A SW/NE profile of Crater T. (**a)** The location of the profile. (**b**) The elevation profile. The white sediment is exposed at the lowest elevations, around -1150m.

Based on the images from 2007 and 2013 at Crater T and 2008 and 2013 at Site N, there is no change in dune or ripple crests. It is important to note that at Crater T, the HiRISE images have very different incident angles, making geo-referencing difficult and therefore direct change detection imperfect. Figure 16 shows the same location in Crater T with no visible difference in the sediment patterns, topography, or morphology. Change detection was also performed on the dune crests and ripples at Site N, where there was no noticeable change.

(**a**) (**b**)

Figure 16. The same location in ESP (2013) (**a**) and PSP (2007) (**b**) HiRISE images. Although the fields of view are not geolinked, no noticeable differences are visible.

Comparing small but steep changes in elevation to the exposures of sediment layers did not show a correlation between types of sediment and slope changes. Figure 17 shows slight steps in the slope shape that mimic the changes in sediment color, although the sediment layers are much thinner than these steps seem to show.

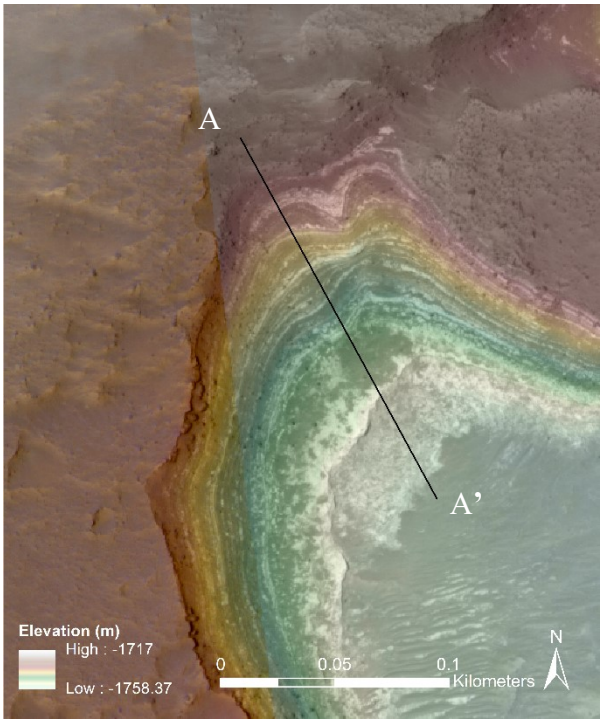

(**a**)

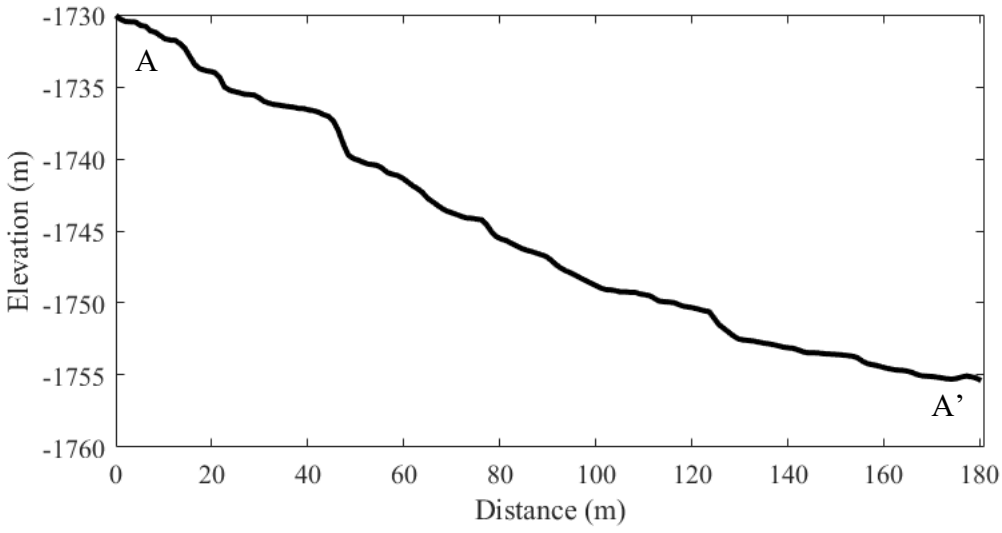

(**b**)

Figure 17. Elevation profile (**b**) of the white and brown sediment layers with the HiRISE image. (**a**) The HiRISE image with elevation overlay shows changes in elevation where the colors change. There are multiple layers within each step of elevation.

Drop-off profiles were tested at all possible changes in elevation at Crater T based on the DEM and HiRISE image; those with distinguishable drop-offs in the interpolated elevation profile were mapped and recorded (Figure 18). The shoreline analysis for Crater T showed multiple drop-off elevations (Table 2). Distinct drop-offs were measurable around the floor of Crater T, with some elevations clustered around -1730, -1757, and -1775 meters, but with considerable drop-offs also measured between the clusters.

Table 2: Drop-off elevations within Crater T.

Elevation (meters)
-1723
-1727
-1730
-1730
-1733
-1737
-1737
-1745
-1747
-1751
-1753
-1757
-1757
-1761
-1764
-1775
-1775
-1777

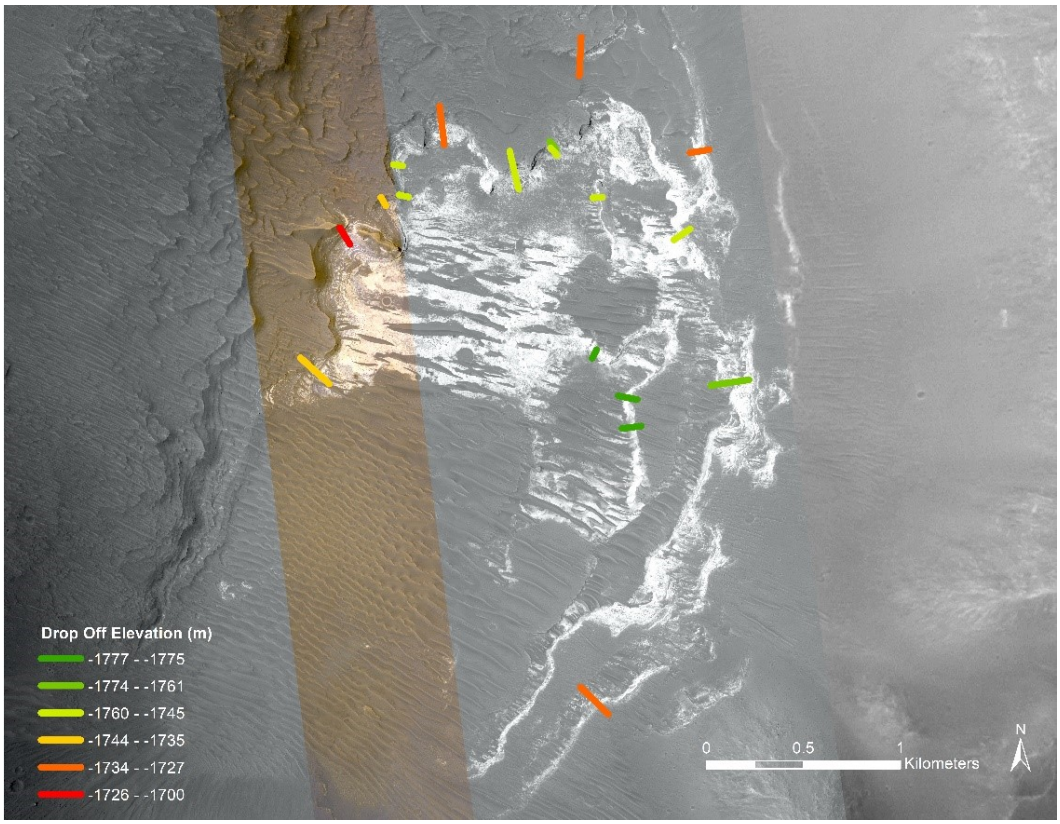

Figure 18. Location for drop-off profile measurements in Crater T.

Dune Pattern Analysis

Visual interpretation of the dune fields at Site N and Crater T show a mix of dune width, height, and shape. Crater T especially has dunes with spatially different patterns within the same dune field. Both sites have no visible craters in the lower and partially shielded basins. Visual inspection of satellite imagery and analysis of dune profiles suggest that the dunes within both study sites are linear (longitudinal) dunes. This classification was made based on the dune length, crest sinuosity, and symmetrical dune profile (Figure 19b). Linear dunes imply a parallel wind regime.

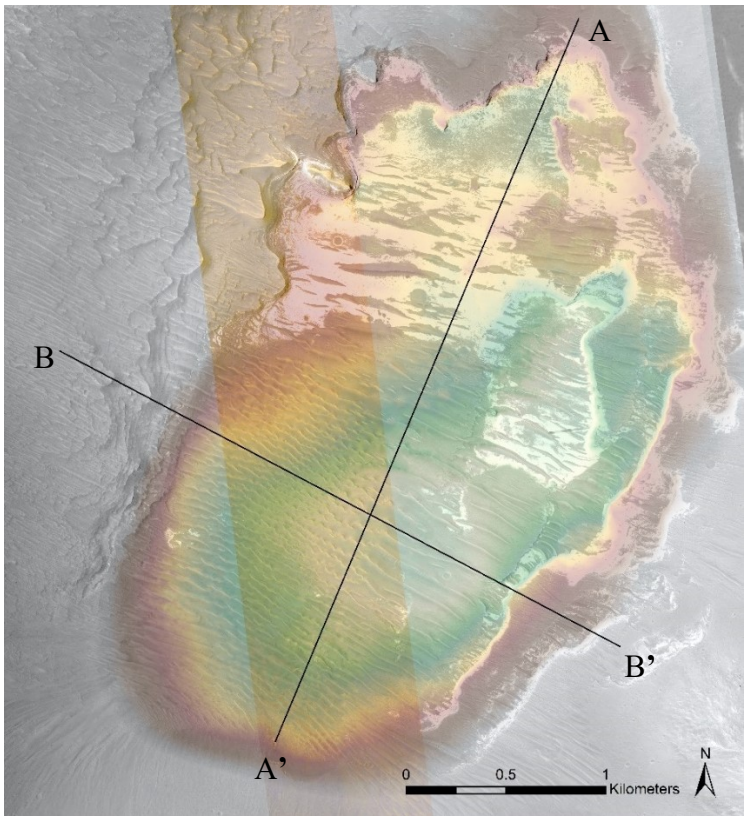

(**a**)

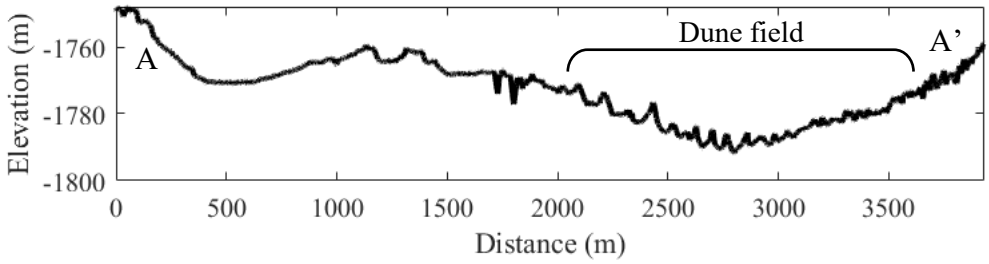

(**b**)

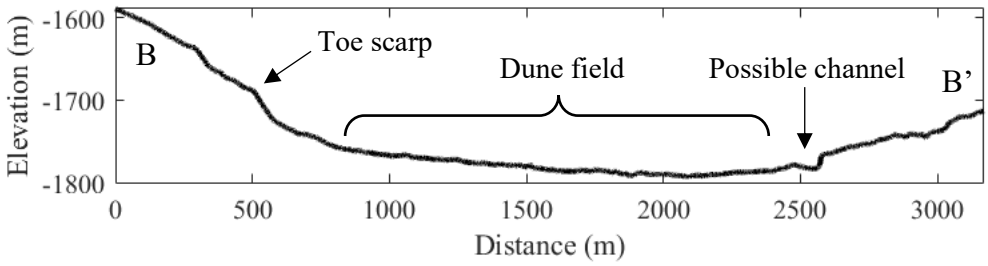

(**c**)

Figure 19. Elevation profiles of the floor of Crater T. (**a**) The location of the profiles. (**b**) The elevation profile of the N/S line. Some dunes are visible in the profile. (**c**) The elevation profile of the E/W line. The collapsed wall toe scarp is visible, as well as a possible channel.

Sinuosity was measured at both study sites using the polylines drawn over dune crests (Figure 20 and 21). The dunes at Site N had an average sinuosity of 1.03, a range of 1.00 to 1.09, and a standard deviation of 0.02. These numbers show very straight dunes, especially compared to the data at Crater T.

Further statistics were measured at Crater T, as listed in Table 3.

Table 3: Descriptive statistics for dunes at Crater T.

Measure	Mean	Standard Deviation	Range
Length	178.78 m	158.91 m	13.32 – 1173.59 m
Sinuosity	1.07	0.05759	1.00 – 1.38
Distance between dunes	43.81 m	20.79 m	1.98 – 126.83 m
Distance between defects	56.984 m	38.212 m	19.58 – 318.25 m
Elevation	-1775.53 m	8.05 m	-1790.33 – -1752.58 m
Direction (east is 0°)	-25.58°	12.79°	-75.58 – 33.89°
Dune height	1.76 m	1.00 m	0.40 – 7.47 m

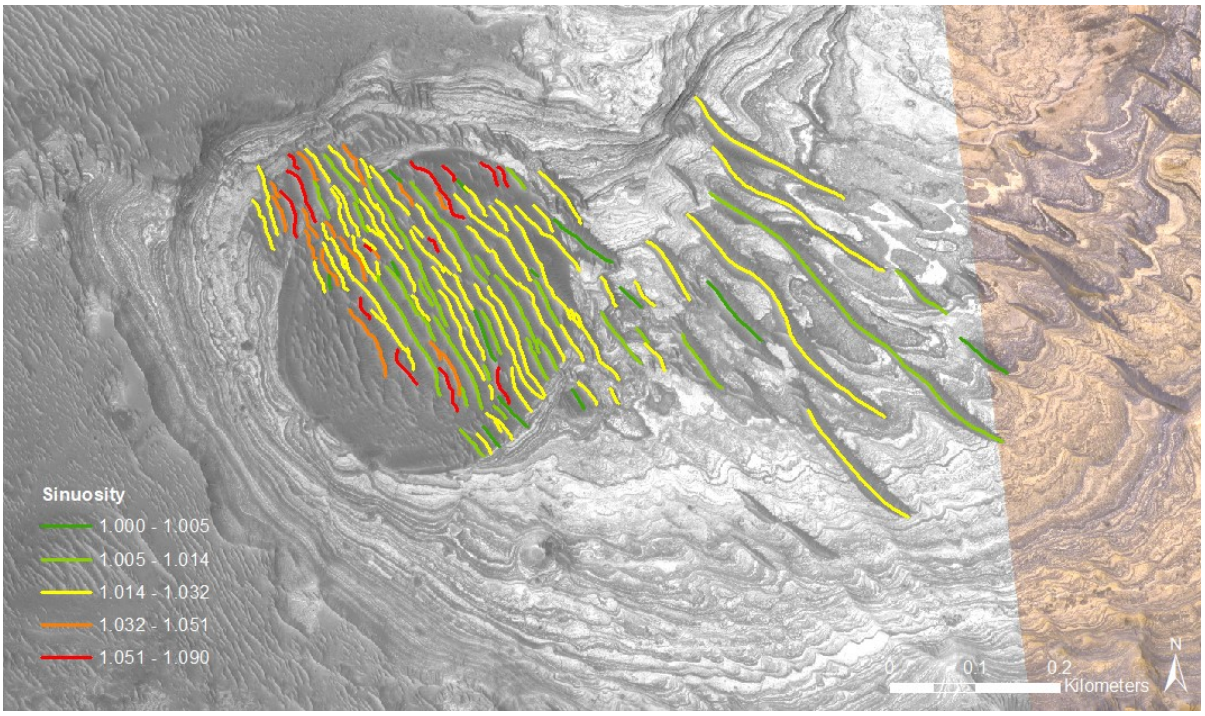

Figure 20. The dune crest polylines at Site N, where each color is delta ½ standard deviation. Yellow dunes are within one standard deviation of the mean sinuosity.

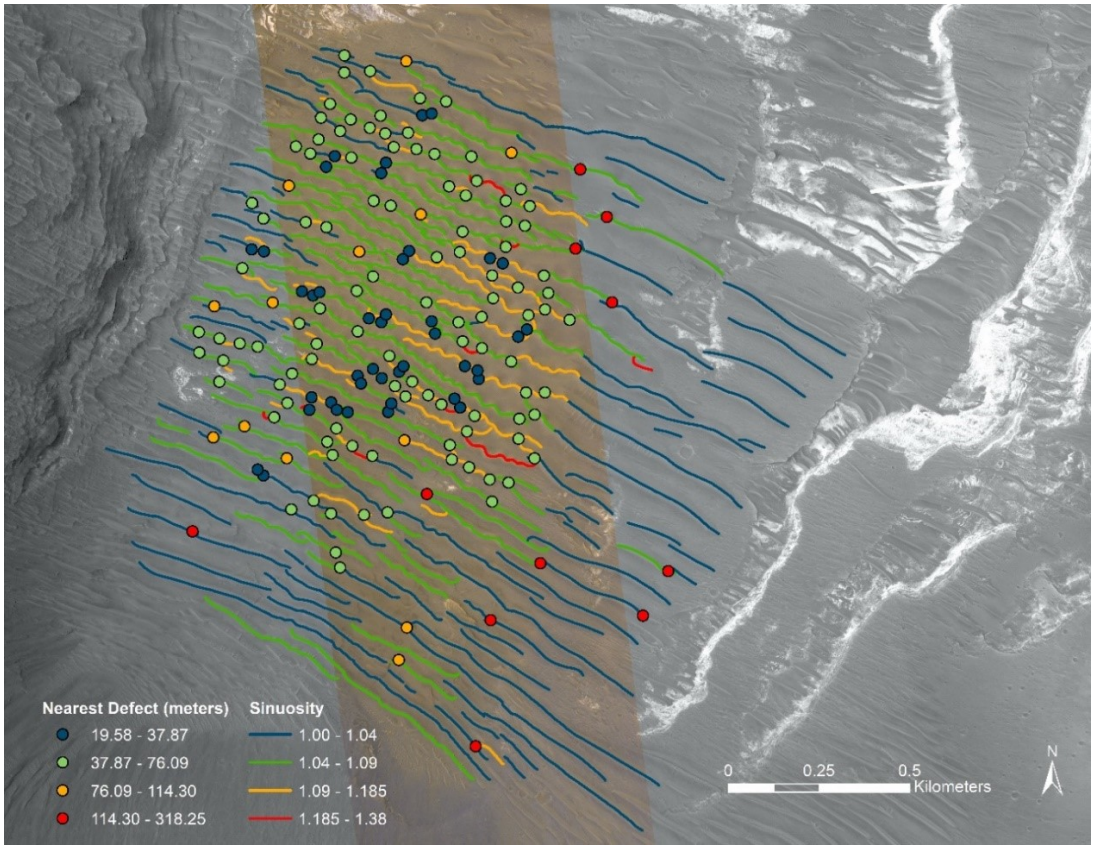

Figure 21. The dune crest polylines and dune defect points at Crater T. Symbolized by standard deviation from the mean, where green dunes and green defects are within one standard deviation of the relative mean.

Most of the dunes run in the northeast/southwest direction at an angle of -25.58°, where due east is 0°, as seen in Figure 22. At Crater T, the shortest dunes, which often stretch between longer dunes, were the most sinuous, as seen in Figures 21 and 23a. Shorter dunes also had more variability in direction (Figure 23b). Dune defects were closer together around the shorter dunes and the more sinuous dunes.

The relative height of the dunes were compared with the other dune variables (Figure 24). This data was developed using the HiRISE DEM, which contained imperfections. Dunes less than 3 meters had a large range of sinuosities but dunes above 4 meters were often straighter (Figure 24b). If dunes were closer together, they were shorter; further distances between dunes had more variability in dune height (Figure 24c and 25).

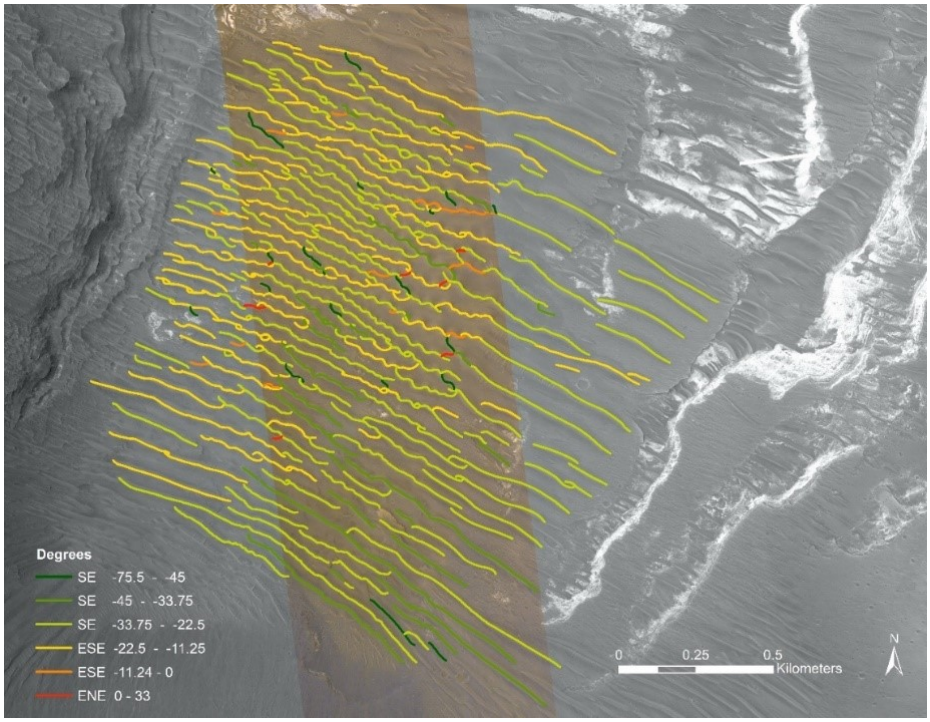

Figure 22. Dune crest lines at Crater T symbolized by degrees away from 0°, where 0° is east/west oriented, or parallel to the equator.

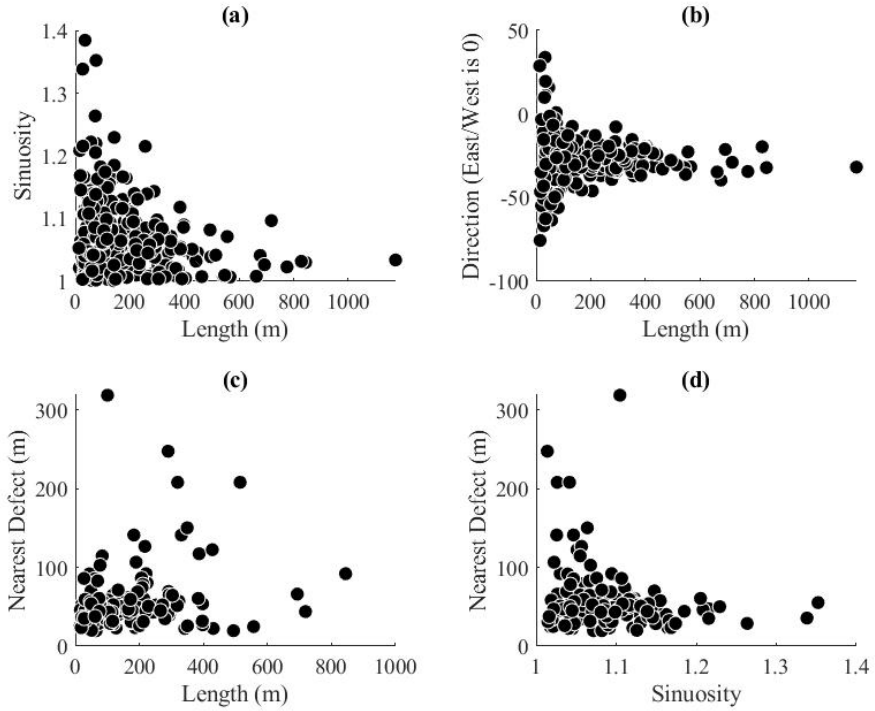

Figure 23. Relationships between (**a**) dune length and sinuosity, (**b**) direction, and (**c**) nearest defect, and (**d**) sinuosity and nearest defect at Crater T.

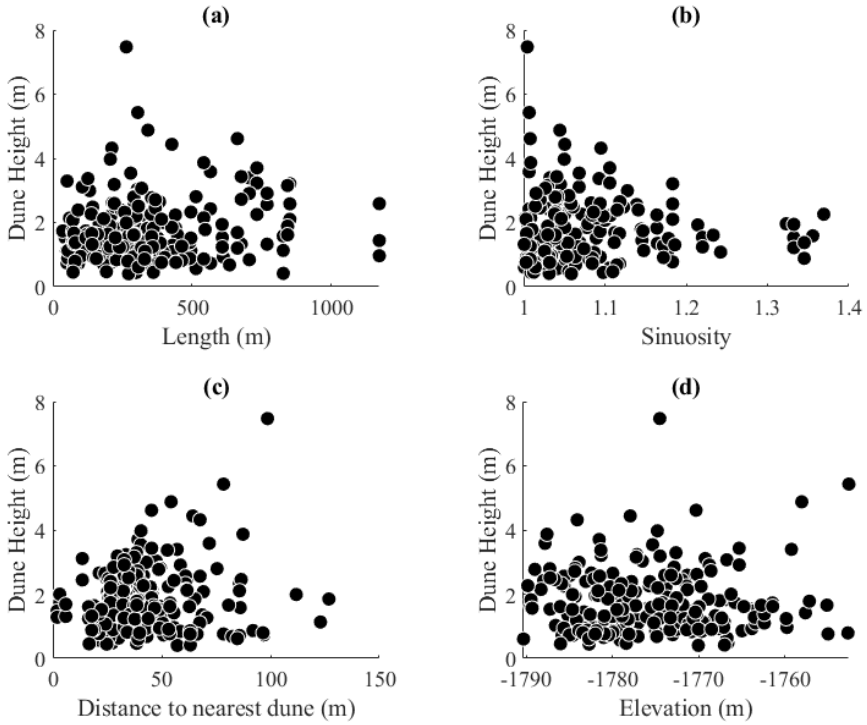

Figure 24. Relationships between (**a**) dune length, (**b**) sinuosity, (**c**) nearest dune, and (**d**) elevation and dune height at Crater T.

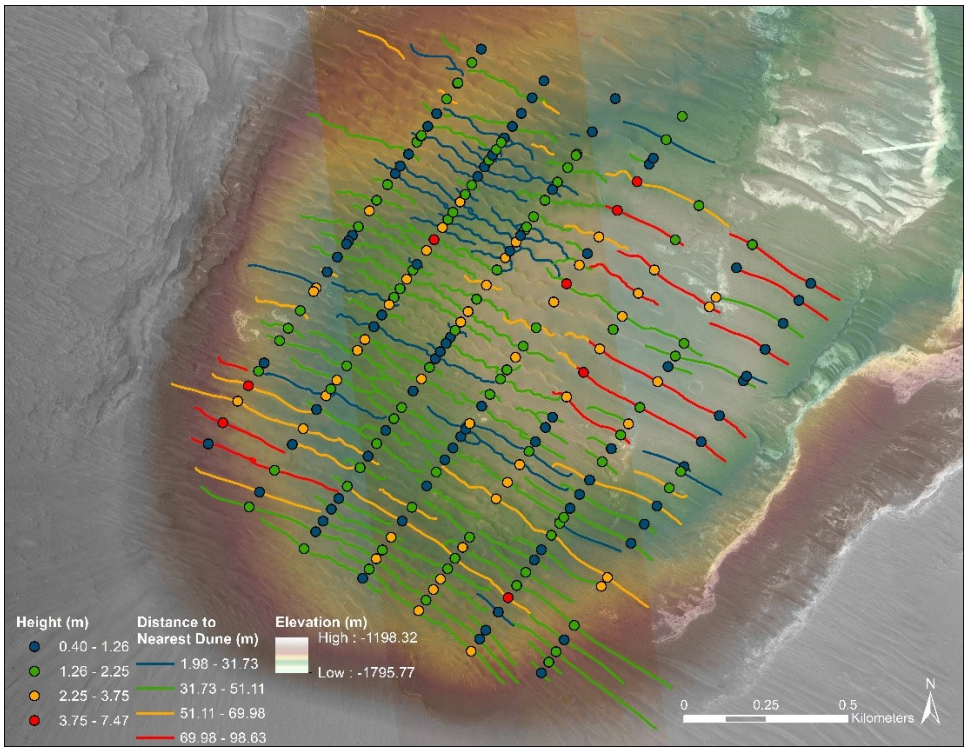

Figure 25. Map of dune height measurement points over the dune crest lines at Crater T, symbolized by distance to the nearest dune. Shorter dunes are often closer together.

Spectrometry and Mineral Analysis

At both Site N and Crater T, there were 5 spectral signatures for brown sediment and 5 spectral signatures for white sediment, each ranging from 0.03 to 2.6 micrometers in wavelength. These were exported into ASCII text files and opened in spreadsheet processing software, where the signature for each sediment type at each site was averaged and the VNIR and IR curves combined (Figure 26). The spectral signature for the white sediment at both sites have a higher reflectance than the brown sediment and more pronounced absorption features, but all of the absorption features are at the same wavelengths for both brown and white sediments: around 0.66, 1.4, 1.96, 2.0, and 2.06μm.

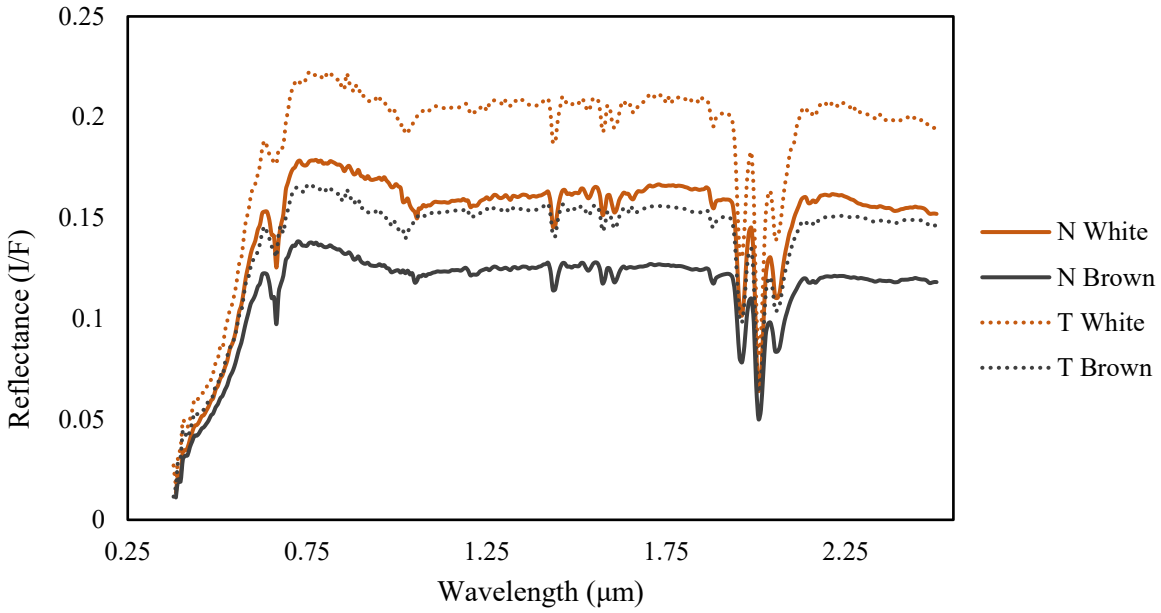

Figure 26. Spectral signatures for brown and white sediment at Site N and Crater T, based on averaged ROI signatures. Relatively, the difference between the brown and white sediments at each site is very similar, but the scale of reflectance at Crater T is higher.

The Spectral Analyst tool in ENVI 5.5 was used to compare each averaged spectral signature to the JPL Mineral library (Tables 4-7). The spectral data for the sediments had very low matching scores for minerals in the JPL library; this is likely due to an issue of reflectance scale. Spectral libraries from the CRISM Mineral Library and USGS were also compared: they too had

Table 4. Spectral Analysis of the averaged white sediment spectrum at Site N.

Library Spectrum	Match Score
Hematite	0.089
Ferroaxinite	0.080
Nontronite	0.079
Galena	0.077
Chalcocite	0.072

Table 5. Spectral Analysis of the averaged brown sediment spectrum at Site N.

Library Spectrum	Match Score
Trona	0.144
Ferroaxinite	0.143
Nontronite	0.132
Ulexite	0.130
Galena	0.129

Table 6. Spectral Analysis of the averaged white sediment spectrum at Crater T.

Library Spectrum	Match Score
Hematite	0.114
Nontronite PS-6B	0.108
Nontronite PS-6D	0.069
Trona	0.064
Ulexite	0.046

Table 7. Spectral Analysis of the averaged brown sediment spectrum at Crater T.

Library Spectrum	Match Score
Nontronite PS-6B	0.121
Hematite	0.119
Trona	0.087
Nontronite PS-6D	0.086
Magnesiochromite	0.082

an issue with reflectance scale but still matched absorption feature wavelengths and curve shape. Because of the low match score for each sediment type, direct conclusion is not feasible. However, when comparing the spectral signatures of the top matched minerals, many of them also have notable absorption features at 1.4 µm and near 1.96 µm, including nontronite, ulexite, and trona (Figure 27).

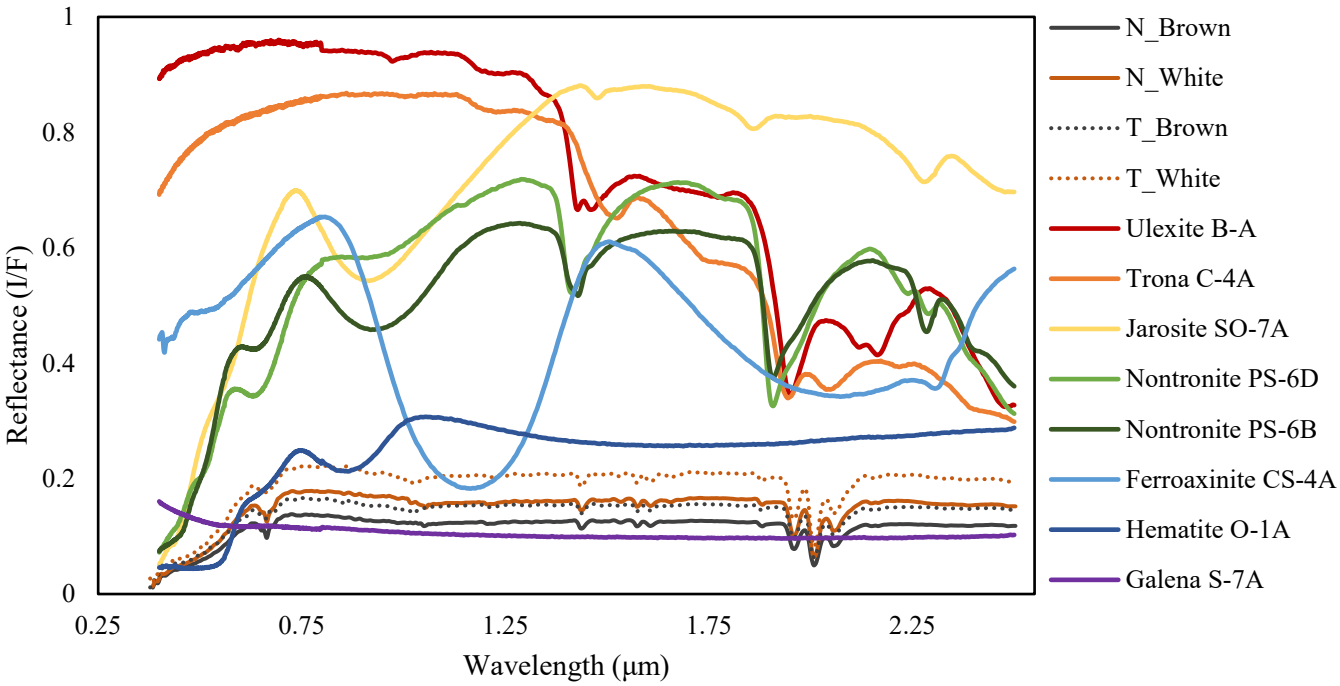

Figure 27. The spectral signatures of the most common mineral matches to both the white and brown sediments at Site N and Crater T.

CHAPTER IV

DISCUSSION

Combining a thorough analysis of the mineralogy with geomorphic and topographic data better quantifies the layered deposits at Site N and Crater T. A detailed understanding of the formation environments depends on a complete analysis of various minerals, landforms, and structures.

Geomorphology

Compiling the variables in the topography and geomorphology studies yield a snapshot of the more recent history of the study sites. The basins in which both exposures of white and brown sediment layers sit are consistent with the collapse formation model of the Orson Welles Chaos: as the subsurface aquifer drained, the surface collapsed. The relative lack of possible flow channels in and out of the study sites could have trapped standing water. The sediment layers have many tens of meters of exposed layering with countless alternations. Because each of the layers of brown and white sediment appears completely horizontal and flat, it is possible that these layers were formed by minerals precipitating out of liquid water inside the crater.

The walls of Crater T appear to have steep drop-offs around the basin floor (seen in Figure 19 at 500 and 2500 meters), but topographic profile analysis showed multiple elevations for drop-offs. If cliffs were caused by shoreline erosion, the level of standing water was not stable, or was rising and falling over time. Water could have been sitting in the aquifer at the time of collapse or it could have flowed north intermittently from Ganges Chasma, creating multiple layers.

Looking directly at the walls of exposed layers, the steps in the topography are comparable to solifluction and creep on Earth, but those processes do not necessarily fit with the model of recent lithification and movement of the sediment. The alternating sediment layers are thinner than

steps in the profile line (Figure 17), so it is unlikely that differences in sediment composition and physical properties created the steps or that there are different rates of erosion or weathering between the white and brown sediments. The dunes at both sites notably only contain brown sediment, but perhaps the sand supply for these dunes is not directly from the exposed sediment layers.

Silvestro et al. (2010) studied ripple migration over barchan dunes at Nili Patera, which has a more consistent elevation than the study sites in this investigation but is not too far from the equator and therefore might see wind patterns similar to those in the Orson Welles Chaos. Mars has notable windstorms, but there is limited evidence for bedform migration, as seen in the stagnant dunes of Crater T and Site N. Silvestro et al. (2010) found that, in Nili Patera, saltation is frequent enough to stop a stabilizing crust from forming. At Site N and Crater T, the HiRISE images taken approximately 5 years apart do not show any signs of dune form or ripple migration, although the lack of impact cratering still implies the dunes in the basins have been recovered much more recently than the dunes elsewhere.

Away from the basins, both study sites show dunes with impact cratering and possible weathering (Figure 28); this supports the hypothesis that these dunes may be lithified and have been eroded by wind during the last climatic era of Mars. Causes of lithification have not been identified, nor does the nearby weathered surface explain the isolation of the recent sediment movement. Figure 28 appears to indicate northwestern winds in the floor of Crater T, which is consistent with wind direction for the nearby linear dunes.

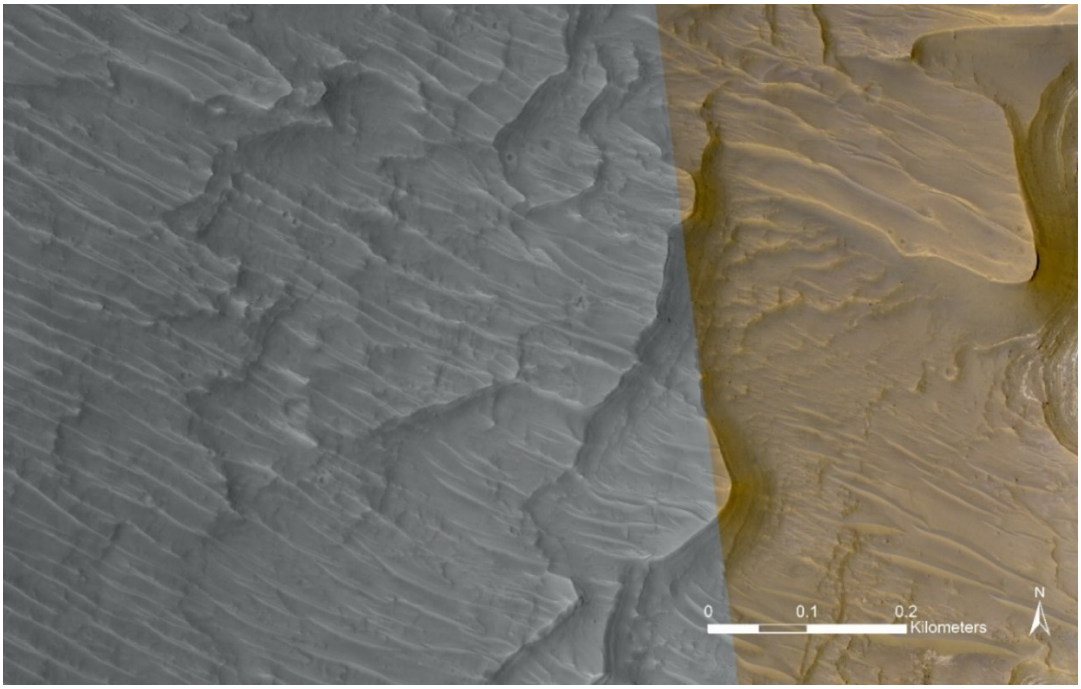

Figure 28. The surface directly to the west of the white sediment layers at Crater T, where there are frequent small impact craters.

In a 2005 study by Kocurek and Ewing, it was found that a consistent wind regime would yield a simple dune pattern. They found that when crests terminations reorient, it translates through the length of the dune. Site N has a consistent dune pattern, indicating a more consistent wind regime, but reorientation might be seen in the more complex region of Crater T, implying that a shift in wind regime caused the complex dune area. Figure 29 shows how dunes with a sinuosity greater than 1.57 correlate to a dune crest orientation concentrated closer to near -30° (northwest/southeast) (this relationship is also seen by comparing dune parameters in Figures 21 and 22, particularly in the northwest corner of the dune field). The complexity of the dunes in Crater T are marked by the changes in sinuosity and dune defect density. The complex dunes look similar to seif dunes on Earth, which are caused by multiple wind directions, and have elongated,

sharps-crested ridges that often consist of successions of oppositely oriented, curved slip faces that give a sinuous or chainlike appearance to the dune crest.

Based on the Kocurek and Ewing (2007) wind regime study, the change in dune crest orientation (Figure 22), the northwest clusters of defects (Figure 21), and the relationship between dune crest orientation and sinuosity (Figure 29), it is possible that the change in dune pattern in the northwest corner of the Crater T dune field is due to both a change of wind direction and an increase in sand supply. The dunes are composed of brown sediment, which means the sediment supply must be brown sediment. It is likely that this sediment is not from the layered floor of Crater T, but possibly from the crater wall or outside the crater.

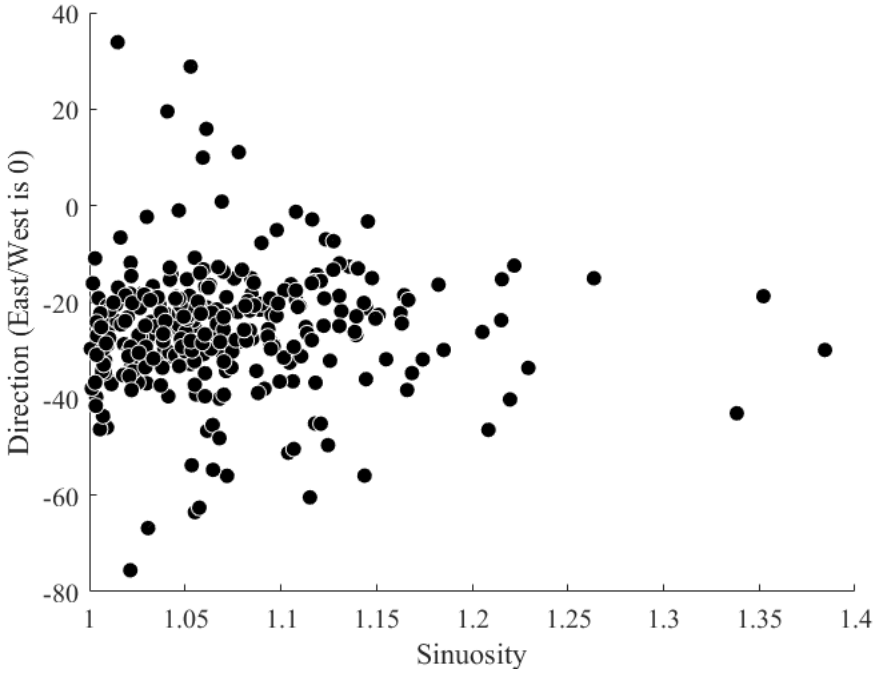

Figure 29. Relationship between dune crest orientation and sinuosity at Crater T.

The dune pattern analysis done at Crater T yielded data that is comparable to data on linear dunes by Lancaster (2009). Lancaster (2009) found that most dune patterns are regular, as seen in statistics about dune features. When comparing dune height and distance between dunes, Lancaster (2009) found a correlation that is apparent in the data from Crater T (Figure 30). This indicates that the linear dunes at Crater T do follow similar regular patterns as linear dunes on Earth. Work on these patterns will continue to compare the dune and wind behavior on Mars to linear dune fields on Earth. If the linear dune patterns on Earth and Mars are similar here, further studies can explore other parameters such as wind direction, defects, and sand supply.

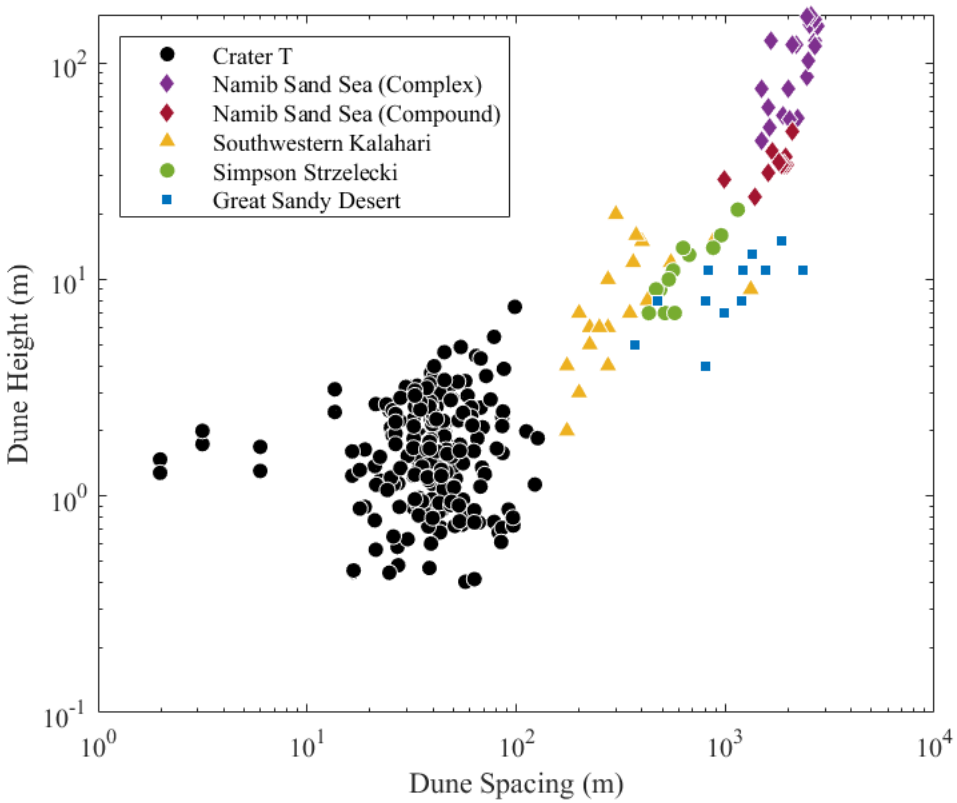

Figure 30. Dune spacing versus dune height at Crater T compared to Earth data of linear dunes from Lancaster (2009), plotted logarithmically.

Spectrometry and Mineral Analysis

Hematite is the best matched mineral in three of the four sediment spectral signatures, which aligns with the history of hematite study on Mars (Christensen, Morris, Lane, Bandfield, & Malin, 2001). The mineral layers at Site N and Crater T might be comparable to banded iron formations and may imply the existence of liquid surface water, but the spectral matching is still very imprecise. Low matching scores between observed spectral signatures and published spectral libraries signify the inherent difficulty in determining the mineralogy of both sites. Potential sources of uncertainty could be attributed to spatial resolution of the hyperspectral system which limits selection of pure pixels and increases the potential of these sites to contain weathered sediments rather than single-mineral exposed bedrocks.

Nonetheless, nontronite was found to have matching scores on all four of the sediment signatures. Nontronite, trona, and ulexite all had similar absorption features to the sediment spectral signatures and are all formed in hydrous environments on Earth. Nontronite is an iron rich phyllosilicate and smectite group member; it also matches the spectral readings of Wintzer et al. (2011), who was looking for Fe/Mg-rich phyllosilicates. Wintzer et at. (2011) noted that the Fe/Mg-rich phyllosilicates are analogous to interbeds within layers of flood basalts and that the two locations of these layers are at different elevations. On Earth, nontronite, a clay mineral, can be a weathering product of basalts and biotites or formed by precipitation of iron and silicon rich hydrothermal fluids (Anthony, Bideaux, Bladh, & Nichols, 2001). At Site N and Crater T, the nontronite might imply the existence of water breaking down a basaltic parent regolith to form the sediment. Because there was little spectral difference between the brown and white sediments, this implication can be applied to the larger, brown sediment-covered Chaos. The existence of water, at least at the subsurface, is consistent with the current formation model of the Orson Welles Chaos.

JHUAPL created derived data products analyzing mineral families in each CRISM data set (Figures 31 and 32). In these selected images, the regions of white sediment at both Site N and Crater T are highlighted for Fe/Mg-rich phyllosilicates and hydrated sulfates or clays. These highlighted regions of chemical differences support the low match score data collected in this study and give confidence to the identification of water related minerals.

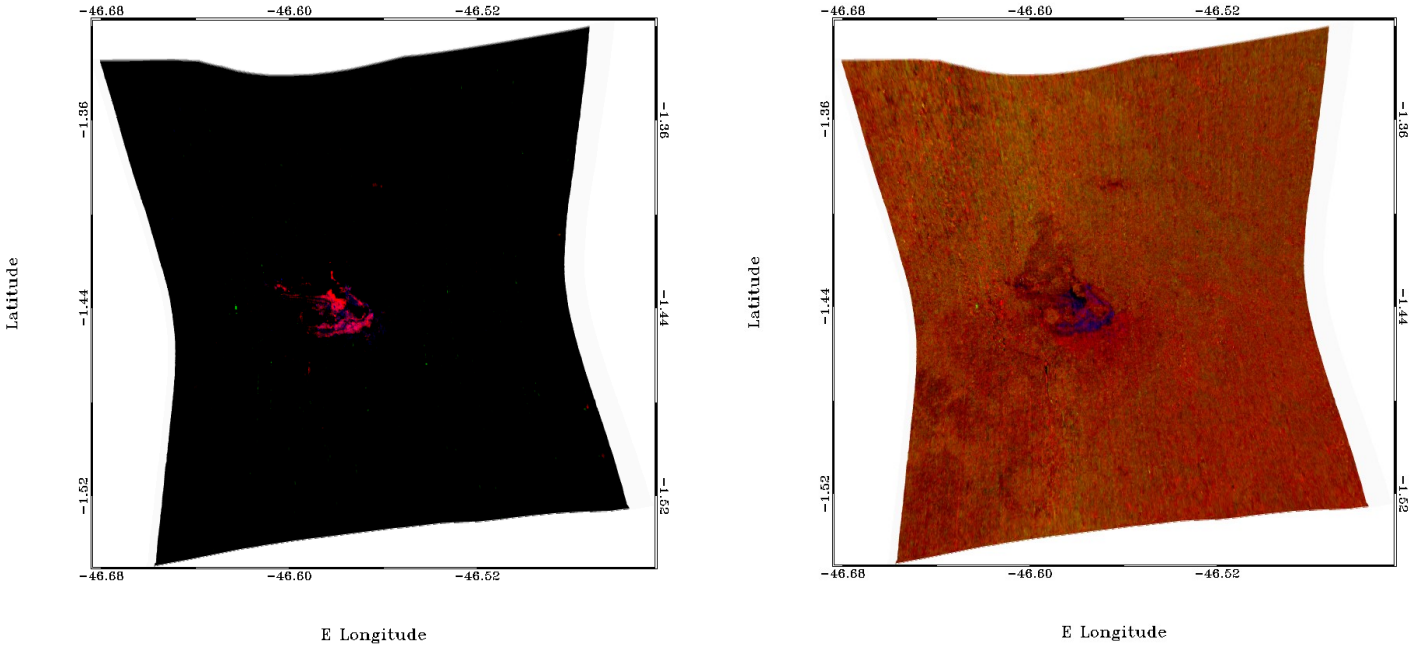

Figure 31. Selected derived data products for visible and near infrared wavelengths of Site N. Image **(a)** looks for hydroxylated silicates. Red represents Fe/Mg phyllosilicates; green represents Al phyllosilicates or hydrated glass; blue represents hydrated sulfates, clays, glass, or water ice. Image **(b)** looks for bound water. Red represents water-containing minerals; green represents monohydrated sulfates or water ice; blue represents hydrated sulfates, clays, glass, or water ice. (NASA & JHUAPL, n.d.)

Although the Spectral Analyst data for this study is inconclusive, there is evidence that the white sediment located at Site N and Crater T may have been exposed to surface water throughout

their histories. Both Site N and Crater T are in relatively low elevations and the location of the white sediment is almost exactly at the lowest point in each basin—right where liquid water would pool if it existed. The lack of white sediment exposures anywhere else in the Chaos, even in other relative basins, may be due to water flow patterns, sediment transport and burial, localized mineral abundances, or additional unknown factors.

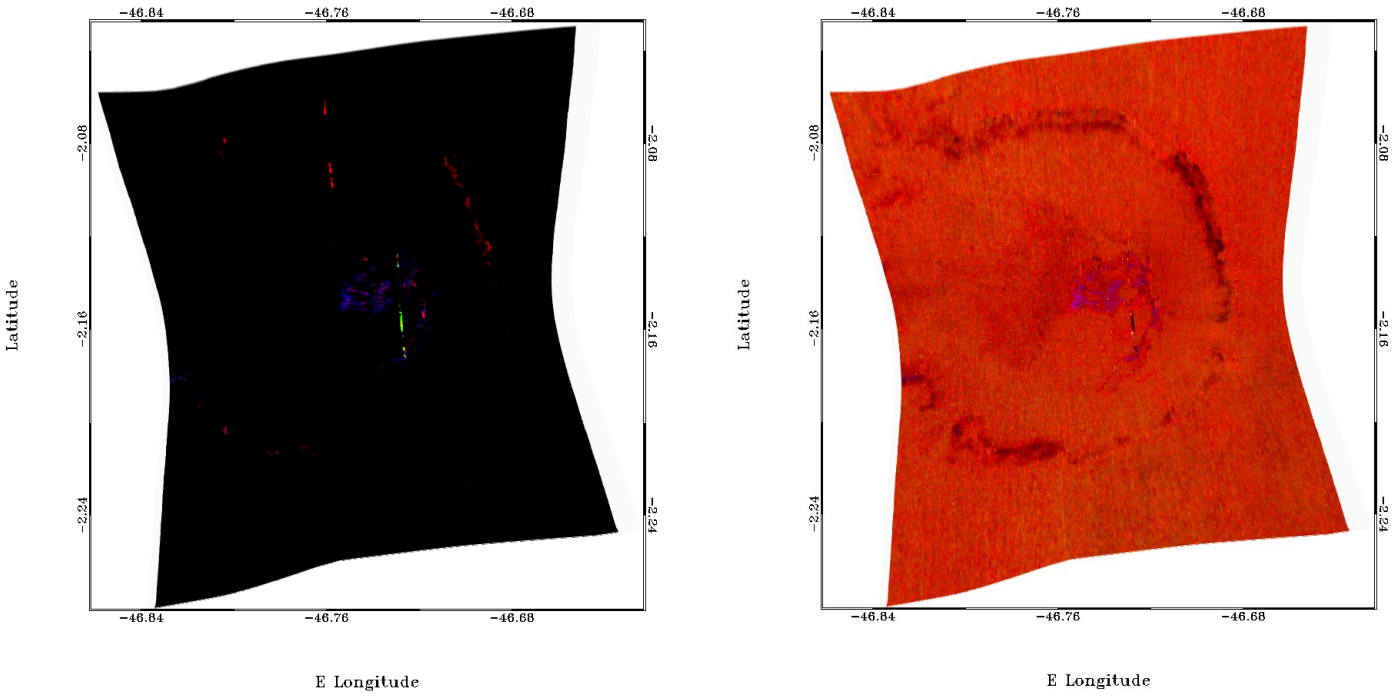

Figure 32. Selected derived data products for visible and near infrared wavelengths of Crater T. Image **(a)** looks for hydroxylated silicates. Red represents Fe/Mg phyllosilicates; green represents Al phyllosilicates or hydrated glass; blue represents hydrated sulfates, clays, glass, or water ice. Image **(b)** looks for bound water. Red represents water-containing minerals; green represents monohydrated sulfates or water ice; blue represents hydrated sulfates, clays, glass, or water ice. (NASA & JHUAPL, n.d.)

Formation Hypotheses

The last objective of this project was to combine the remotely sensed spectrometry and geomorphology data into a hypothesis of formation for the two layered deposits in Crater T and Site N. A thorough study of the features within the Orson Welles Chaos and the smaller layered deposits make a much more detailed hypotheses possible.

Without quantitative evidence, this study can only make hypotheses about the role of water in the formation of the white and brown sediment layers. Taking the uncertainties associated with the data into account, this study presents the following formation hypothesis: the sediments associated with Site N and Crater T and their particular layering style is a result of the precipitation of minerals in standing surface water. The layers at Crater T and Site N may have been formed by evaporites—mineral analysis was inconclusive but the minerals that matched the spectral data in all four analyses are hydrous minerals. Drop-offs in elevation could be interpreted as shorelines of water levels that fluctuated constantly. There is evidence for a possible channel on the floor of Crater T based on the topography (around 2500 meters in Figure 19b), but any liquid in that channel did not leave polygonal fractures or clear shorelines. The exposure of the layers at Site N is nearly 700 meters higher than the floor of Crater T, and further complicate this hypothesis. The horizontality of the layers at both sites is the key piece of physical evidence for the existence of liquid water inside the crater. Of course, additional evidence might be buried in the sand.

CHAPTER V

CONCLUSION

This study aimed to understand the relationship of the different geomorphic aspects of these study sites to hypothesize about the formation of the white sediment layers and understand its past. The relationship of geomorphic features at Site N and Crater T does not definitively explain the layered sediment but does not rule out the possibility of standing water at both study sites after the collapse of the Orson Welles Chaos.

When looking at the topography of the study sites, it was clear that the sediment layers were formed after the collapse of the larger region. No distinctions were found between the physical characteristics of the brown sediment versus the white sediment. There is enough brown sediment supply to form dunes and the lack of white sediment dunes was not proven to be a result of different weight or lithification potential.

Studying the brown sediment dunes showed a change of wind regime on the floor of Crater T, as sinuosity and dune defects increased in the northwestern corner of the dune field. Further study of the wind patterns in Crater T will aid in understanding the more modern processes affecting the crater, including how the scarp is eroding and exposing or covering the white sediment layers.

This study was unable to decipher the exact mineral family for the brown or the white sediment at either study site due to the inconsistency of the data. Notable absorption features were found at 1.4 μm and near 1.96 μm, which are similar to nontronite, ulexite, and trona, which form in hydrous environments on Earth. Although the data in this study cannot be used to draw precise or robust conclusions, the minerals found in the Orson Welles Chaos align with the current formation models and are promising leads for future studies with more complete data.

Future work on the Orson Welles Chaos and dune pattern analysis at other locations on Mars will aim for study sites with data that is less error prone. The equatorial location of the Orson Welles Chaos will allow any findings to be applied to common rover landing sites at the Mars equator. Understanding the composition and formation of these two deposits can lead to a better understanding of the geologic and hydrologic history of Mars.

BIBLIOGRAPHY

Anthony, J. W., Bideaux, R. A., Bladh, K. W., & Nichols, M. C. (2001). *Handbook of Mineralogy*. Retrieved from http://www.handbookofmineralogy.org/search.html?p=all

Bridges, N. T., Ayoub, F., Avouac, J.P., Leprince, S., Lucas, A., & Mattson, S. (2012). Earth-like sand fluxes on Mars. *Nature*, *485*(7398), 339–342. doi: 10.1038/nature11022

Cabrol, N. A., Grin, E. A., & Dawidowicz, G. (1997). A Model of Outflow Generation by Hydrothermal Underpressure Drainage in Volcano–Tectonic Environment, Shalbatana Vallis (Mars). *Icarus*, *125*(2), 455–464. doi: 10.1006/icar.1996.5625

Chojnacki, M., Banks, M. E., Fenton, L. K., & Urso, A. C. (2019). Boundary condition controls on the high-sand-flux regions of Mars. *Geology*, *47*(5), 427–430. doi: 10.1130/G45793.1

Christensen, P. R., Engle, E., Anwar, S., Dickenshied, S., Noss, D., Gorelick, N., & Weiss-Malik, M. (2009). JMARS - A Planetary GIS. *AGU Fall Meeting Abstracts*, *22*, IN22A-06.

Christensen, P. R., Morris, R. V., Lane, M. D., Bandfield, J. L., & Malin, M. C. (2001). Global mapping of Martian hematite mineral deposits: Remnants of water-driven processes on early Mars. *Journal of Geophysical Research: Planets*, *106*(E10), 23873–23885. doi: 10.1029/2000JE001415

Dohm, J. M., Hare, T. M., Robbins, S. J., Williams, J.P., Soare, R. J., El-Maarry, M. R., … Maruyama, S. (2015). Geological and hydrological histories of the Argyre province, Mars. *Icarus*, *253*, 66–98. doi: 10.1016/j.icarus.2015.02.017

Ewing, R. C., Kocurek, G., & Lake, L. W. (2006). Pattern analysis of dune-field parameters. *Earth Surface Processes and Landforms*, *31*(9), 1176–1191. doi: 10.1002/esp.1312

Fenton, L. K., Bandfield, J. L., & Ward, A. W. (2003). Aeolian processes in Proctor Crater on Mars: Sedimentary history as analyzed from multiple data sets. *Journal of Geophysical Research: Planets*, *108*(E12). doi: 10.1029/2002JE002015

Horvath, D. G., & Andrews-Hanna, J. C. (2017). Reconstructing the past climate at Gale crater, Mars, from hydrological modeling of late-stage lakes. *Geophysical Research Letters*, *44*(16), 8196–8204. doi: 10.1002/2017GL074654

JMARS. (n.d.). JMARS Website by Mars Space Flight Facility, Arizona State University. Retrieved April 15, 2020, from https://jmars.asu.edu/

Kocurek, G., & Ewing, R. C. (2005). Aeolian dune field self-organization – implications for the formation of simple versus complex dune-field patterns. *Geomorphology*, *72*(1), 94–105. doi: 10.1016/j.geomorph.2005.05.005

Lancaster, N. (1994). Dune Morphology and Dynamics. In A. D. Abrahams & A. J. Parsons (Eds.), *Geomorphology of Desert Environments* (pp. 474–505). doi: 10.1007/978-94-015-8254-4_18

Lancaster, N. (2009). Dune Morphology and Dynamics. In *Geomorphology of Desert Environments* (pp. 557–596). doi: 10.1007/978-1-4020-5719-9_18

NASA, & JHUAPL. (n.d.). CRISM Data Products—Site N. Retrieved February 18, 2020, from http://crism-map.jhuapl.edu/details.php?data=frt_webmap_polygons&shape=7809&x=-46.564&y=-1.433905

NASA MGS. (n.d.). Mars Global Surveyor. Retrieved January 23, 2020, from NASA's Mars Exploration Program website: https://mars.nasa.gov/mars-exploration/missions/mars-global-surveyor

NASA MRO. (n.d.). Mars Reconnaissance Orbiter Instruments. Retrieved January 23, 2020, from https://mars.nasa.gov/mro/mission/instruments/

Ritter, D. F., Kochel, C., & Miller. (2011). *Process Geomorphology* (5th ed.). Waveland Press Inc.

Silvestro, S., Fenton, L. K., Vaz, D. A., Bridges, N. T., & Ori, G. G. (2010). Ripple migration and dune activity on Mars: Evidence for dynamic wind processes. *Geophysical Research Letters*, *37*(20). doi: 10.1029/2010GL044743

Sullivan, R., & Kok, J. F. (2017). Aeolian saltation on Mars at low wind speeds. *Journal of Geophysical Research: Planets*, *122*(10), 2111–2143. doi: 10.1002/2017JE005275

Wintzer, A. E., Allen, C. C., & Oehler, D. Z. (2011, January 1). *Phyllosilicate Deposits in Shalbatana Vallis*. Retrieved from https://ntrs.nasa.gov/search.jsp?R=20110004906